

DESIGN, SIMULATION, FABRICATION, AND CHARACTERISTICS
OF TERAHERTZ METAMATERIAL DEVICES

by

LEE A. BUTLER

SEONGSIN M. KIM, COMMITTEE CHAIR

PATRICK KUNG
PATRICK LECLAIR

A THESIS

Submitted in partial fulfillment of the requirements
for the degree of Master of Science
in the Department of Electrical and Computer Engineering
in the Graduate School of
The University of Alabama

TUSCALOOSA, ALABAMA

2012

Copyright Lee A. Butler 2012
ALL RIGHTS RESERVED

ABSTRACT

In recent years metamaterials have been extensively researched and show strong potential to improve many devices. Metamaterials offer significant advantages over conventional materials because their properties depend mainly on geometrical design rather than composition. This important property allows metamaterials to be geometrically scaled such as to operate in any desired spectral range. Specifically, implementation of metamaterials into devices targeted to operate in the terahertz regime could greatly improve fields such as chemistry, biology, security, and medicine.

In this work, terahertz metamaterials have been studied and novel devices have been designed and demonstrated. In particular, this work is focused mainly on metamaterial structures designed to absorb incident radiation. These absorber devices show promise for use in areas such as imaging and interference reduction applications. Both narrow-band and broadband absorber devices have been designed using simulations and fabricated using standard photolithography and electron deposition techniques.

DEDICATION

This thesis is dedicated to everyone who supported me throughout my academic career. Especially, I wish to dedicate it to my family and friends whose constant aid and encouragement has allowed me to accomplish this goal.

LIST OF ABBREVIATIONS AND SYMBOLS

<i>THz</i>	Terahertz (1×10^{12} Hz)
<i>PDE</i>	Partial Differential Equation
<i>FEA</i>	Finite Element Analysis
<i>DOF</i>	Degree(s) of Freedom
<i>SRR</i>	Split-Ring Resonator
<i>EC-SRR</i>	Edge-Coupled Split-Ring Resonator
<i>ERR</i>	Electric Ring Resonator
\vec{E}	Electric Field Intensity in Volts per meter (V/m)
\vec{H}	Magnetic Field Intensity in Amperes per meter (A/m)
\vec{D}	Electric Flux Density in Coulombs per square meter (C/m^2)
\vec{B}	Magnetic Flux Density in Webers per square meter (Wb/m^2)
\vec{J}	Electric Current Density in Amperes per square meter (A/m^2)
ρ	Electric Charge Density in Coulombs per cubic meter (C/m^3)
\vec{S}	Complex Poynting Vector

ACKNOWLEDGMENTS

I would like to thank all professors, colleagues, family, and friends who have helped me in any way with this research work. I wish to express the utmost gratitude to my advisors, Dr. Margaret Kim and Dr. Patrick Kung for all of their support and guidance throughout my graduate study. They have provided me with much direction and guidance which has allowed me to perform the research necessary for the compilation of this thesis.

I also wish to thank Dr. Patrick LeClair for his time, support of my work, and willingness to serve on my thesis committee. Additionally, I would like to thank my colleagues, Shawn and Eli, for providing experimental data necessary for this work. Finally, I want to thank my family and friends for all of their support throughout the assembly of this work.

CONTENTS

ABSTRACT.....	ii
DEDICATION.....	iii
LIST OF ABBREVIATIONS AND SYMBOLS	iv
ACKNOWLEDGMENTS	v
LIST OF TABLES.....	viii
LIST OF FIGURES	ix
1 INTRODUCTION	1
1.1 Project Goal and Thesis Outline	2
2 METAMATERIALS	3
2.1 Engineering Electromagnetic Response	5
2.2 Split-Ring Resonator.....	6
2.3 THz Metamaterial Absorber	13
2.3.1 Simulation of Previously Reported Designs	15
2.3.2 Proposed Design: Polarization-Insensitive THz Absorber ...	19
2.3.3 Broadband THz Absorber	22
3 FEA SIMULATIONS.....	24
3.1 Simulation Method.....	24
3.2 Results.....	26
3.2.1 Normal Incidence Tests	26

3.2.2 Polarization Sensitivity Tests.....	30
3.2.3 Broad Band Absorption Tests.....	33
4 EXPERIMENTAL MEASUREMENTS	41
4.1 Device Fabrication	41
4.2 Measurement Technique.....	43
4.3 Results.....	44
4.3.1 Normal Incidence Tests	45
4.3.2 Polarization Sensitivity Tests.....	47
5 CONCLUSIONS AND FUTURE WORK.....	49
5.1 Summary	49
5.2 Future Work	49
REFERENCES	51

LIST OF TABLES

2.1 Split-ring resonator geometrical parameters	10
2.2 Geometrical parameters for absorber similar to that proposed by H. Tao	15
3.1 Geometrical parameters for proposed polarization-insensitive absorber	27
3.2 Geometrical parameters for proposed broadband absorbers.....	34
3.3 Geometrical parameters for proposed eight-ring broadband absorbers	38
4.1 Geometrical parameters for fabricated absorber arrays	45

LIST OF FIGURES

2.1 Right-handed and left-handed triplet systems.....	4
2.2 Combinations of material permittivity and permeability	6
2.3 Circular split-ring resonator	7
2.4 Split-ring resonator behavior and equivalent circuit.....	8
2.5 Transmission spectrum of EC-SRR	11
2.6 Electric response of EC-SRR structure and current in both rings	12
2.7 Metamaterial THz absorber unit cell	14
2.8 Absorption spectra with electric and magnetic response at resonance.....	16
2.9 Metamaterial THz absorber unit cell similar to that proposed by Y. Ma et al.....	17
2.10 Absorption spectra of closed ring absorber structures with electric responses at resonance	18
2.11 Surface current on the closed rings of square-ring and circular-ring absorbers	19
2.12 Polarization-insensitive THz metamaterial absorber structure	20
2.13 Various field polarization angles incident upon a THz metamaterial structure.....	21
2.14 Rotations to test absorber sensitivity to various incidence angles	21
2.15 Designed structure for THz metamaterial broadband absorber	22
2.16 Circular ring design structure for THz metamaterial broadband absorber.....	23

3.1 The finite element method process of meshing and refining	25
3.2 Absorption spectra with electric and magnetic response at resonance.....	28
3.3 Effect of dielectric layer thickness on absorption.....	29
3.4 Electric and magnetic field vectors solved using FEA at normal incidence.....	30
3.5 Absorption spectra resulting from variance in polarization angles	31
3.6 Absorption spectra resulting from various incidence angles	32
3.7 Absorption spectra of square-ring and circular-ring broadband absorbers	35
3.8 Square eight-ring broadband absorber structure	36
3.9 Circular eight-ring broadband absorber structure	37
3.10 Absorption spectra of eight-ring broad band absorbers	39
4.1 Metamaterial absorber fabrication process	42
4.2 Optical microscope images of fabricated metamaterial absorber array	43
4.3 Experimental setup for study of metamaterial absorbers.....	44
4.4 Experimental absorption spectra of fabricated absorber arrays	46
4.5 Absorption spectrum of Y' showing discrepancy correction	47
4.6 Absorption spectra resulting from experimental measurements of polarization variations	48

CHAPTER 1

INTRODUCTION

Metamaterials have a strong potential to greatly impact the electromagnetic response of many materials and devices. First proposed by V.G. Veselago in 1968 as “left-handed substances”, metamaterials are constructed such that electromagnetic properties are exhibited which do not occur in nature. Research focusing on the electromagnetic response of metamaterials has generated fascinating devices such as invisibility cloaks and superlenses [1-4]. These devices are able to be realized due to un-natural material behavior which results from engineering material characteristics. Metamaterials can be characterized by effective complex permittivity $\varepsilon(\omega) = \varepsilon'(\omega) + i\varepsilon''(\omega)$ and permeability $\mu(\omega) = \mu'(\omega) + i\mu''(\omega)$. By carefully constructing materials to take advantage of the ability to adjust $\varepsilon(\omega)$ and $\mu(\omega)$, it is possible to create metamaterials which exhibit properties such as backward wave propagation and negative index of refraction, $n(\omega) < 0$ [5, 6]. Much unlike conventional materials, electromagnetic properties of metamaterials strongly depend on the structures themselves, much more so than material chemical composition. Typically, metamaterials are composed of periodic arrays of metallic elements designed to exhibit resonant behavior at some desired frequency. Thus, one important feature of metamaterials is their ability to be scaled geometrically in order to achieve desired electromagnetic responses in various frequency ranges. Consequently, metamaterial devices have been realized and demonstrated in spectral ranges from radio and microwave up to infrared and near-optical [7-10].

In this work, the focus is on electromagnetic properties of metamaterials in the terahertz (THz) regime. The terahertz radiation spectrum lies in between radio frequencies and optical frequencies at 0.1-10 THz ($1 \text{ THz} = 1 \times 10^{12} \text{ Hz}$). This translates to a wavelength range of 30 μm - 3 mm. Until recently, little work has been done in the THz range due to its difficulty to produce and manipulate. But many substances have a strong response at terahertz frequencies. Thus, there is a wide variety of applications for devices utilizing THz radiation [11-14] which are promising tools for matter characterization. Unlike radiation in the X-ray frequency range, terahertz radiation is not harmful. This property makes it ideal for use in applications such as non-invasive medical imaging and security screening. Additionally, this low-energy, non-ionizing radiation, is able to penetrate non-conductive materials with low water content, rendering them transparent in the THz range. For this reason, THz radiation can non-invasively and accurately characterize tissues, teeth, DNA, weapons, explosives, and potentially epithelial cancer [15-20]. Thus, terahertz spectroscopy shows promise to greatly impact fields such as chemistry, biology, security, and medicine.

1.1 Project Goal and Thesis Outline

The goal of this work was to design, develop, fabricate, and test novel metamaterial devices. The primary focus was the development and fabrication of novel THz metamaterial absorbers. In Chapter 2, a concise theory of metamaterials is given which is the basis for the subsequent THz absorber designs. Chapter 3 introduces the finite element analysis solution method used for device development and presents simulation data. The experimental measurement technique and results are presented in Chapter 4. Finally, the conclusion and future work are covered in Chapter 5.

CHAPTER 2

METAMATERIALS

Metamaterials have potential to open up a whole new class of tools and instruments as the fundamental units of extraordinary devices such as superlenses, invisibility cloaks, sensors, filters, and antennas to name a few. The basic theory of modern metamaterials was first proposed in a well-known paper by V.G. Veselago in 1968 but such materials were not realized until the end of the 20th century. Here, a brief overview of metamaterial theory is presented. The familiar governing expressions for all electromagnetic waves, Maxwell's equations, are expressed here in the differential form [21]:

$$\nabla \times \vec{E} = - \frac{\partial \vec{B}}{\partial t} \quad (\text{Faraday's Law of Induction}) \quad (2.1)$$

$$\nabla \cdot \vec{B} = 0 \quad (\text{Gauss's Law for Magnetism}) \quad (2.2)$$

$$\nabla \times \vec{H} = \frac{\partial \vec{D}}{\partial t} + \vec{J} \quad (\text{Ampere's Circuital Law}) \quad (2.3)$$

$$\nabla \cdot \vec{D} = \rho \quad (\text{Gauss's Law}) \quad (2.4)$$

It is also worth noting that these expressions contain information expressing the conservation of charge in a relation known as the equation of continuity:

$$\nabla \cdot \vec{J} = - \frac{\partial \rho}{\partial t} \quad (\text{Conservation of Charge}) \quad (2.5)$$

The electromagnetic constitutive relationships in simple matter are the following:

$$\vec{D} = \epsilon \vec{E}$$

$$\vec{B} = \mu \vec{H}$$

$$\vec{j} = \sigma \vec{E}$$

where σ is the medium, or material, *conductivity* usually expressed in Siemens per meter (S/m).

These expressions must be satisfied for all electromagnetic fields at all points in space and for all points in time. Also, these expressions along with relations (2.1) – (2.4) exhibit the importance of electric permittivity and magnetic permeability to the electromagnetic response of metamaterials.

The vast majority of naturally occurring materials are characterized by positive permittivity and permeability values ($\epsilon > 0, \mu > 0$). One exception is plasma, which can exhibit negative permittivity. Also, metals can exhibit negative permittivity at optical frequencies and some ferromagnetic materials may exhibit negative permeability at microwave frequencies.

Metamaterials, however, can be constructed to exhibit negative permittivity and negative permeability. If permittivity and permeability are simultaneously negative ($\epsilon < 0, \mu < 0$), the result is a negative index of refraction ($n < 0$). In this case, the material is known as left-handed media and the phenomenon of backward wave propagation is exhibited. Shown in Figure 2.1, this is one significant property of metamaterials that makes possible such devices as superlenses.

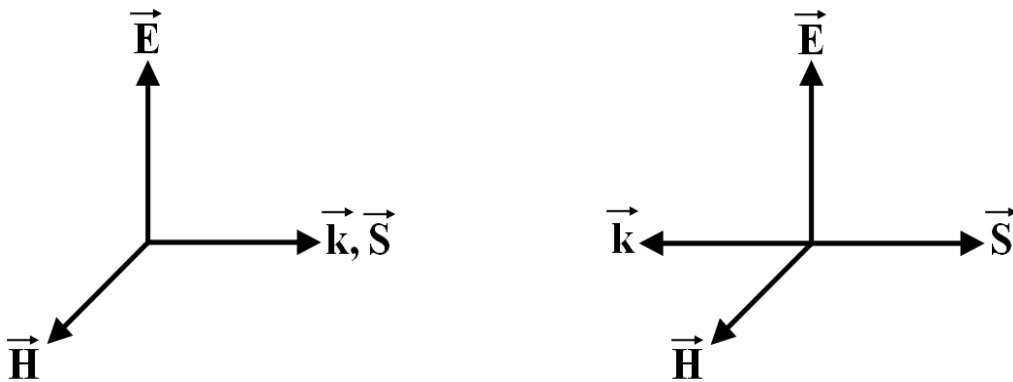


Figure 2.1 (left) Right-handed triplet system: Poynting vector and wave vector in same direction.
(right) Left-handed media: Poynting vector and wave vector in opposite directions

2.1 Engineering Electromagnetic Response

Due to the importance of effective material permittivity and permeability, we may now explore how to control these parameters in order to develop novel devices. In electromagnetism, permittivity is defined to be the ability of a material to polarize in response to an external electric field. Simply put, it is a measure of how well a material transmits an electric field. Similarly, permeability is defined to be the ability of a material to magnetize in response to an external magnetic field. We now know that in order to develop such interesting devices as perfect lenses and invisibility cloaks, precise control of permittivity and permeability values must be achieved. Consider the diagram in Figure 2.2 showing each possible combination of permittivity and permeability. It turns out that negative effective permittivity may be achieved by a very simple periodic array of metallic wires. Achieving negative permeability, however, is a bit more complicated requiring, for instance, an array of split-ring resonators. These resonators are the fundamental element in D. Schurig's cloaking design and will be discussed in the following section. The response of these split-ring resonator arrays (as with any metamaterial structure) is highly dependent on size, shape, and electromagnetic wave polarization.

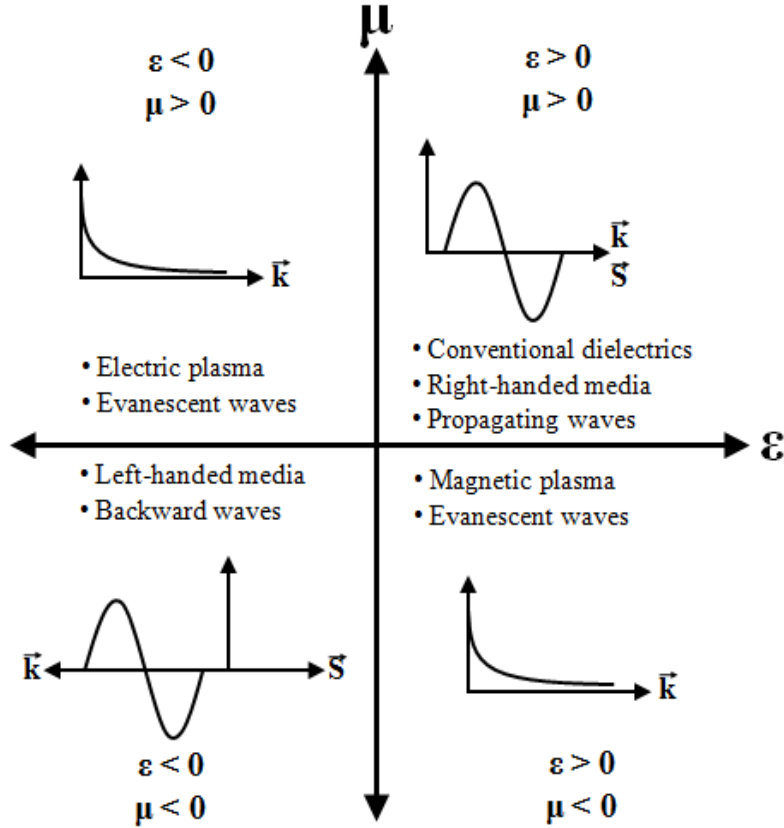


Figure 2.2 Every combination of material permittivity and permeability, and some properties of each

2.2 Split-Ring Resonator

It is well-known that a time-varying magnetic field imposed upon a metallic ring induces an electrical current. This phenomenon was established by Michael Faraday in the nineteenth century. The self-inductance of such a closed metallic ring has been found to be

$$L = \mu_0 r \left[\ln \left(\frac{16r}{d} \right) - 2 \right] \quad (2.6)$$

where r is the radius of the ring and d is the diameter of the ring. For all practical ratios of r/d , the expression (2.6) results in self-inductance values $L \geq \mu_0 r$. Ultimately, the magnetic susceptibility is given as

$$|\chi| \leq \frac{\pi^2}{8} \sim 1 \quad (2.7)$$

Thus, these expressions reveal that no configuration of closed metallic rings can result in a LC resonance or a negative value for effective permeability. LC resonance can be achieved by loading the ring with a capacitor. This arrangement, first proposed by S.A. Schelkunoff, results in a magnetic polarizability expressed as

$$\alpha = \frac{\pi^2 r^4}{L} \left(\frac{\omega_0^2}{\omega^2} - 1 \right)^{-1} \quad (2.8)$$

where ω_0 is the resonance frequency of the equivalent LC circuit formed by the closed ring and the capacitor. The resonance frequency can be calculated by $\omega_0 = \frac{1}{\sqrt{LC}}$ or $f_0 = \frac{1}{2\pi\sqrt{LC}}$.

By quick examination of expression (2.8), it is easy to see that just above resonance frequency the polarizability becomes negative (large negative value). Thus, it can be expected that an arrangement of closed metallic rings loaded with capacitors will produce a negative effective permeability just above the resonance frequency. But fabrication of such a structure designed for operation at microwave and higher frequencies would be difficult. This challenge can be overcome by replacing the lumped capacitance with a distributed capacitance. Known as the split-ring resonator (SRR), this configuration was first proposed by J.B. Pendry in 1999 [22] and is shown in Figure 2.3 (depth not shown).

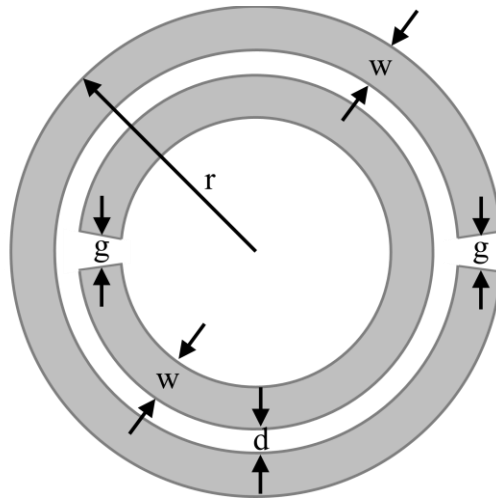


Figure 2.3 Circular split-ring resonator proposed by J.B. Pendry in 1999

Pendry's SRR is able to exhibit resonances at wavelengths that are much larger than the ring diameters. This structure also allows the possibility to fabricate a large series of small rings using common photo-etching techniques which can provide resonances and large negative values of effective permeability. Also, this structure can be scaled down to operate at infrared and optical frequencies. The particular design proposed by Pendry is known as an "edge-coupled SRR" or "EC-SRR" which consists of two concentric metallic rings printed on a microwave circuit board. Having two rings (as opposed to only one), allows this structure to obtain a higher capacitance which results in a stronger resonance. When the EC-SRR is excited by a time-varying magnetic field polarized perpendicular to the plane of the rings, the splits on each ring cause electric current to flow from one ring to the other across the spacing between them. Thus, the spacing (or slot) between concentric rings serves as a distributed capacitance. Additionally, if the electric field is polarized perpendicular to the gaps in the rings, a capacitance is formed in the gaps. Figure 2.4 shows the behavior of the edge-coupled split-ring resonator as well as the EC-SRR equivalent circuit.

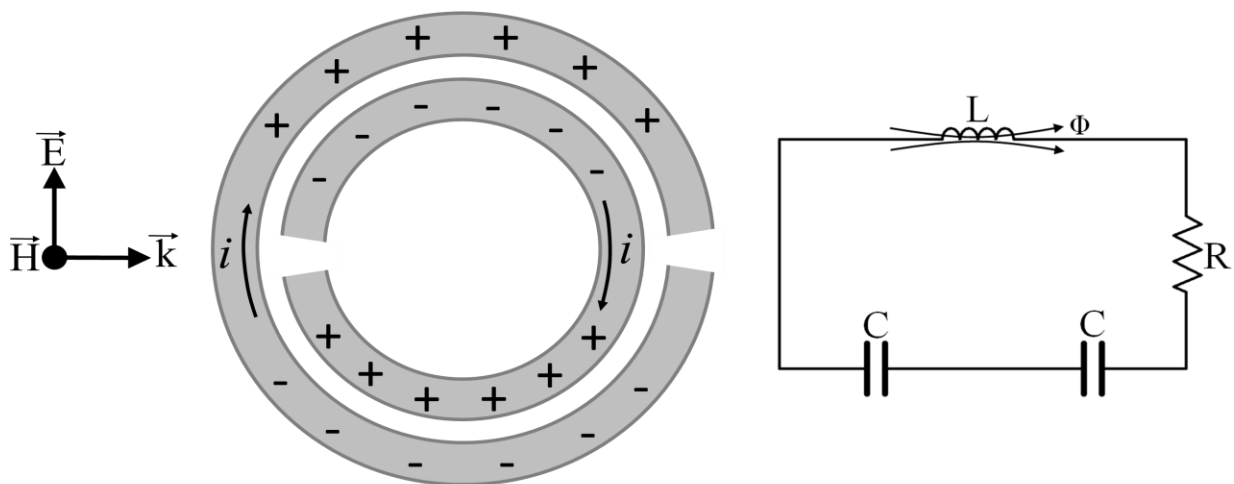


Figure 2.4 Split-ring resonator behavior (left) and SRR equivalent circuit model (right)

In this figure, L represents the self inductance and C represents the capacitance associated with each ring of the EC-SRR. The capacitance value is given as $C = \pi\bar{r}C_{pul}$, where C_{pul} is the per-unit-length capacitance of the EC-SRR and \bar{r} is the mean radius of the EC-SRR configuration. SRR structures can be easily fabricated such that they are arranged in periodic arrays. This enables coupling between individual SRR structures which results in a stronger resonance. The total capacitance of the equivalent circuit is simply the series capacitance of both rings comprising the EC-SRR structure, $C_{tot} = C/2$. If losses are negligible, then this gives the total induced current of the equivalent circuit to be

$$I = \frac{\Sigma_{ext}}{\left(\frac{2}{j\omega C} + j\omega L\right)} \quad (2.9)$$

where Σ_{ext} is the external excitation. This equivalent circuit model is a reasonable representation as long as the outer circumference of the EC-SRR structure is much less than a half-wavelength of excitation source field. That is,

$$2\pi r_1 \ll \frac{\lambda}{2} \quad (2.10)$$

Additional resulting assumptions are that the total current on both rings remains constant and the voltage across both ring splits is also constant. If we let $\Sigma_{ext} = 0$, then (2.9) may be used to solve for the resonance frequency of the EC-SRR. Thus, the resonance frequency is found to be

$$\omega_0^2 = \frac{2}{LC} = \frac{2}{\pi\bar{r}C_{pul}L} \quad (2.11)$$

If the EC-SRR is excited by an external source with polarizations consistent with those shown in Figure 2.4, a strong electric response and a strong magnetic response are excited simultaneously. Importantly, Pendry calculated the effective permeability of this EC-SRR to be

$$\mu_{eff} = 1 - \frac{\pi\bar{r}^2/A^2}{1 - \frac{3L}{\pi^2\mu_0\omega^2 C\bar{r}^3} + i\left(\frac{2d\rho}{\omega\bar{r}\mu_0}\right)} \quad (2.12)$$

where A is the lattice parameter and ρ is the per unit length resistance.

In order to demonstrate the operation of circular split-ring resonators, simulations have been carried out on the EC-SRR structure of Figure 2.3. The geometrical parameters used for the simulations are shown and the values are given in Table 2.1.

Table 2.1 Split-ring resonator geometrical parameters

EC-SRR Geometrical Parameters				
r (μm)	w (μm)	g (μm)	d (μm)	<i>thickness</i> (μm)
15	4	2.44	3	1

When this configuration is excited, surface currents are forced to flow on the edge-coupled rings and the electric field induces a capacitance. Thus, a strong LC response is given at a specific frequency, ω_0 , such that

$$f_0 = \frac{1}{2\pi\sqrt{LC}} \quad (2.13)$$

The transmission spectrum resulting from the response of the simulated EC-SRR structure is shown in Figure 2.5. The transmission is obtained from a two-port system power flow using the following relation

$$\text{Transmission} = \frac{\text{Power transmitted through structure}}{\text{Power incident on structure}} \quad (2.14)$$

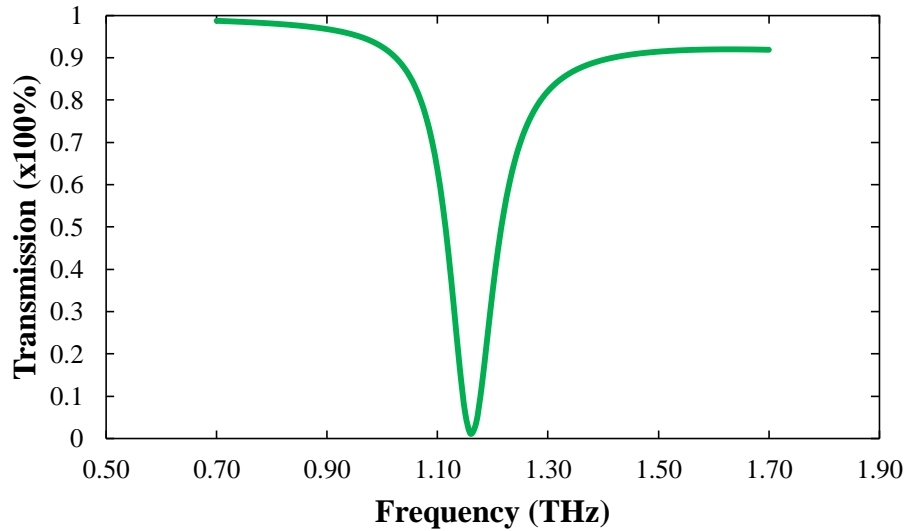


Figure 2.5 Transmission spectrum of circular EC-SRR. Resonance is at 1.16 THz

This EC-SRR was simulated using the finite-element method which will be discussed in the following chapter. The rings were modeled as lossless copper with frequency-independent conductivity $\sigma = 6 \times 10^7$ S/m. The SRR was placed in free-space. The dip in transmission intensity indicates a resonance at $f_0 = 1.16$ THz which corresponds to the LC resonance. The electric and magnetic responses in the edge-coupled ring structure are more clearly visible by making use of the finite element analysis solutions to view the electric field and current. The normal electric field and current is shown in Figure 2.6 for a non-resonance frequency as well as for the resonance frequency.

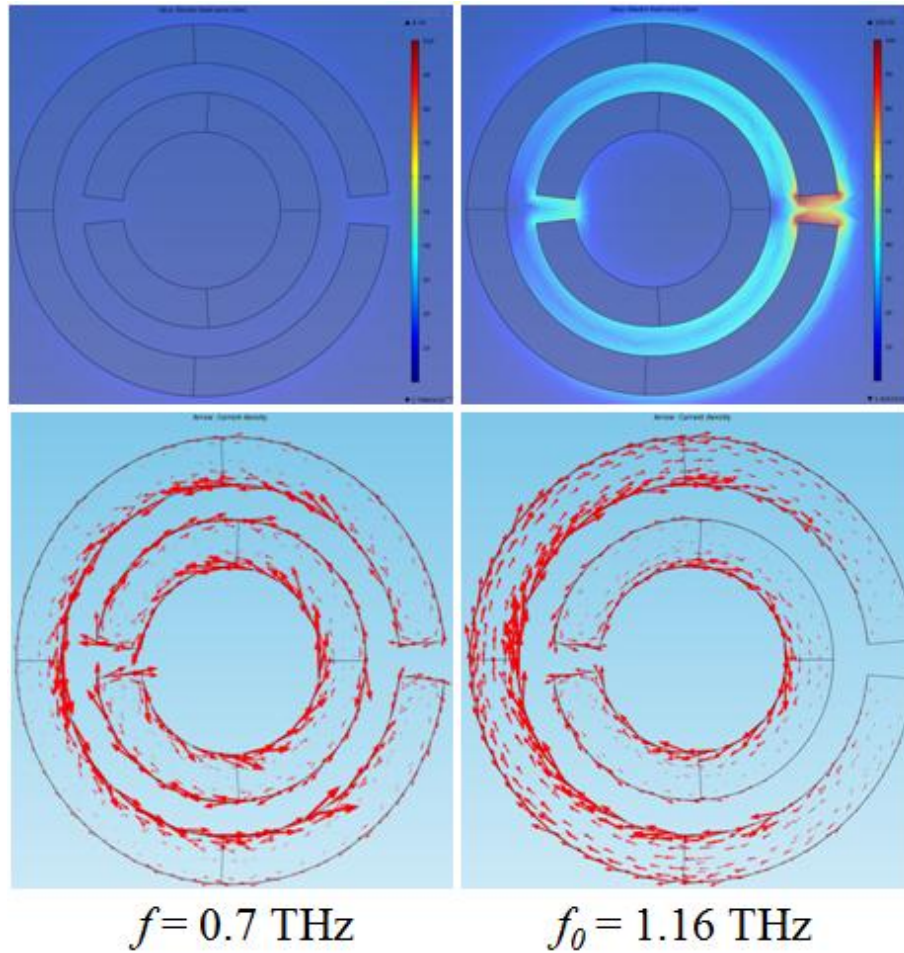


Figure 2.6 Electric response of the EC-SRR structure (top) and current in both rings (bottom) for a non-resonance frequency and at resonance frequency

Thus, at non-resonance frequency (in this case 0.7 THz) no capacitance is formed in the structure so no electric response is exhibited. Additionally, it is interesting to note that the small surface currents are directed in a closed loop about both rings (counterclockwise along the inside and clockwise along the outside). On the other hand, at resonance frequency (1.16 THz) a capacitance is formed in the ring gaps as well as in the area between rings resulting in a strong electric response visible at the top right of Figure 2.6. Also at resonance frequency, notice that the current in the structure is consistent with that shown in Figure 2.4 with the current highly concentrated on the outer ring and directed clockwise.

2.3 THz Metamaterial Absorber

Quite recently, it has been shown that by clever adjustment of $\epsilon(\omega)$ and $\mu(\omega)$, resonant metamaterials which are highly absorbent may be realized [23, 24]. These spectrally selective absorbers show strong potential for use as the fundamental elements in sensor/detector devices such as thermal imagers and explosives detectors as well as interference reduction applications. More specifically, these devices would prove especially beneficial in the THz regime for imaging purposes in the fields of biology and medicine. Metamaterials offer a means of developing tools and instruments for use in the THz range where few electromagnetically responsive materials occur in nature. In order to obtain high absorption, transmission ($T(\omega)$) and reflection ($R(\omega)$) must be simultaneously minimized. The frequency-dependent absorption is defined by $A(\omega) = 1 - T(\omega) - R(\omega)$. Thus, if $T(\omega_0) \approx R(\omega_0) \approx 0$ then the desired high absorption $A(\omega_0) \approx 1$ may be obtained at some resonance frequency, ω_0 . At any other frequency, the absorption will be very small ($A \approx 0$). First proposed and demonstrated at microwave frequencies by N.I. Landy in 2008, metamaterial absorbers consist of two metallic layers separated by a dielectric spacer (some designs include a substrate) [25, 26]. These absorbers allow the incident electric and magnetic fields to be simultaneously absorbed. Consider the absorber unit cell structure shown in Figure 2.7.

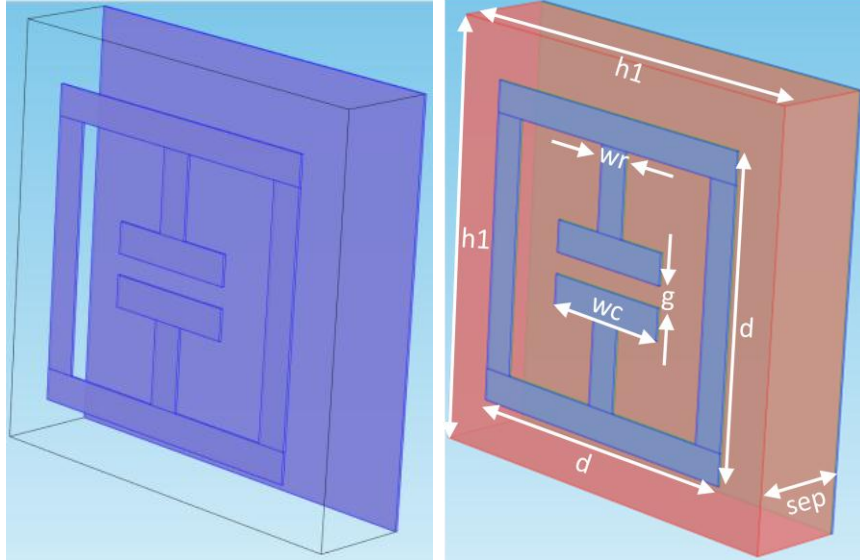


Figure 2.7 Metamaterial THz absorber unit cell

The effective permittivity and permeability are able to be tuned by adjusting the electric and magnetic responses independently. Adjustment of the electric response is achieved by geometrical variations of the top metallic layer known as the *electric ring resonator* (ERR) [27]. Based on the aforementioned split-ring resonator, the ERR is designed to exhibit only an electric response by making use of “plates” to form a capacitance. The magnetic response can be adjusted by changing the spacing between metallic layers since the incident magnetic field couples to these layers. It was mentioned earlier that in order for reflection to be ≈ 0 , the effective impedance of the structure must be matched to that of free-space. Since the back layer of this structure is a continuous ground plane, zero transmission ($T(\omega) = 0$) is ensured for all THz frequencies. Thus, for this configuration only incidence and reflection contribute to the total field. In order for the impedance of the structure to match free-space impedance, permittivity and permeability must be carefully adjusted such that

$$Z = \sqrt{\frac{\mu}{\epsilon}} \approx 1 \quad (2.15)$$

This means that maximum absorption will occur when the relative effective permittivity and permeability are most nearly equal ($\epsilon(\omega_0) \approx \mu(\omega_0)$).

2.3.1 Simulation of Previously Reported Designs

The configuration shown in Figure 2.7 is the basic novel design proposed by H. Tao et al in 2008. This design effectively exhibits near-perfect absorption at THz frequencies. In order to demonstrate the performance of this metamaterial absorber and to validate the accuracy of our simulation method, the design of Figure 2.7 was simulated. The design was modeled with very similar parameters to that tested by H. Tao et al. The metallic layers were modeled as copper and the dielectric layer was modeled as polyimide. Table 2.2 displays geometrical parameters for absorbers to target three different frequencies.

Table 2.2 Geometrical parameters for absorber similar to that proposed by H. Tao

Design	Geometrical Parameters						
	d (μm)	w_r (μm)	w_c (μm)	g (μm)	h_1 (μm)	<i>Metallic Layer Thickness</i> (μm)	sep (μm)
A	35	3.5	15	2.5	47	0.2	8.8
B	30	3	13	2	40	0.2	7.7
C	25	2.5	11	1.5	33.5	0.2	7.1

The simulated absorption spectrum for each variation on the design by H. Tao et al is shown in Figure 2.8. The electric (inset top) and magnetic (inset bottom) responses at resonance are also shown for this design.

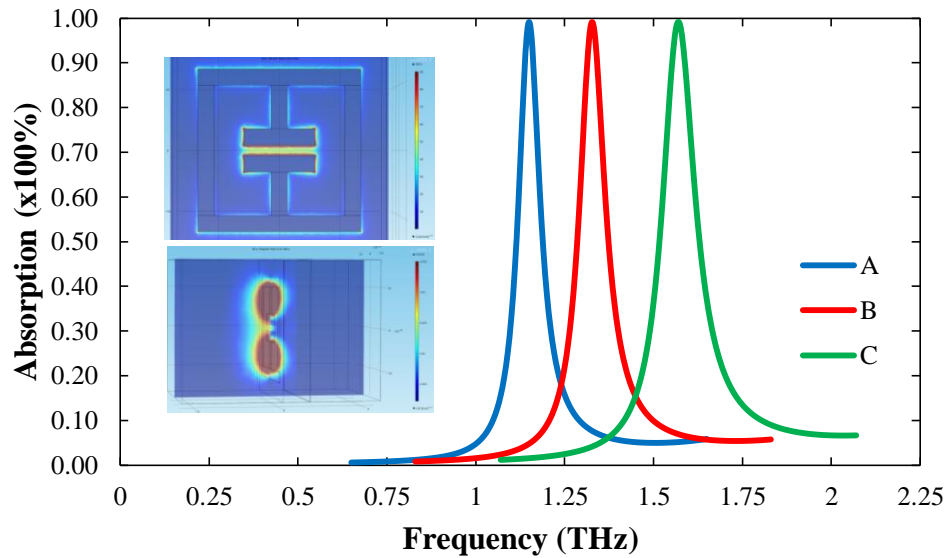


Figure 2.8 Absorption spectra with electric response (inset top) and magnetic response (inset right) at resonance

Thus, designs A, B, and C exhibit absorptions of 99.1%, 99.1%, and 99.2%, respectively. These near-unity absorptions occur at center frequencies 1.15 THz, 1.327 THz, and 1.57 THz for designs A, B, and C, respectively. The absorption peaks offer a full-width-at-half-maximum (FWHM) from 0.07 THz to 0.11 THz making this absorber structure ideal for spectrally-selective imaging applications. An additional metamaterial absorber design of great importance to this work is a structure similar to that of Figure 2.7. Shown in Figure 2.9, this slight variation on a design proposed by Y. Ma et al in 2011 consists of a square closed ring structure and a ground plane separated by a dielectric layer.

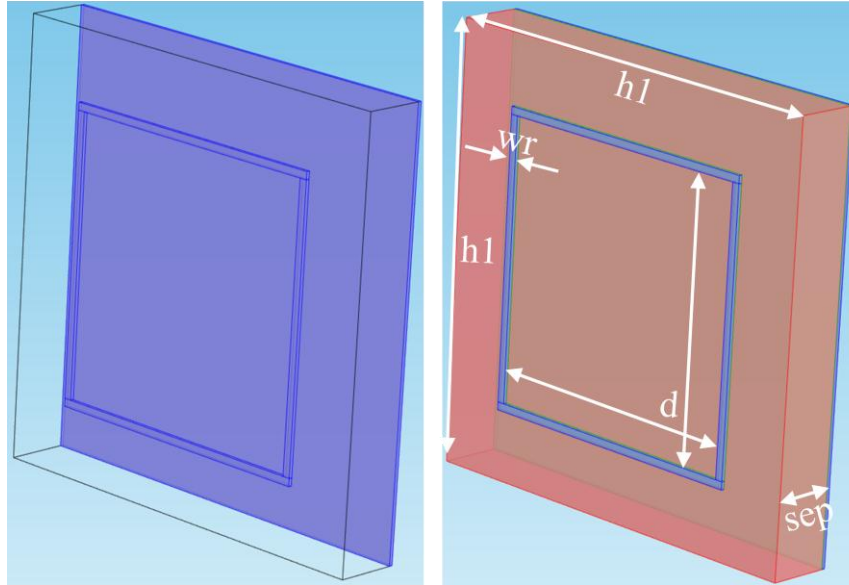


Figure 2.9 Metamaterial THz absorber unit cell similar to that proposed by Y. Ma et al

This design is another spectrally selective near-perfect absorber with copper metallic layers and a polyimide dielectric layer. But the mechanism that produces absorption includes a dipole resonance along the sides of the square ring, rather than a LC resonance as in the previous design. This is precisely the property that supports broad-band absorbers developed in this work, which will be discussed in following sections. As an example of the performance of these structures, Figure 2.10 shows the absorption spectra of the simulated square-ring design as well as a very similar circular-ring design. Also shown is the electric field intensity in each ring (inset) at the resonance frequency. The tested square-ring design has side lengths of $60\ \mu\text{m}$ which is also the diameter of the tested circular-ring design. Each ring is $2\ \mu\text{m}$ wide and $0.4\ \mu\text{m}$ thick.

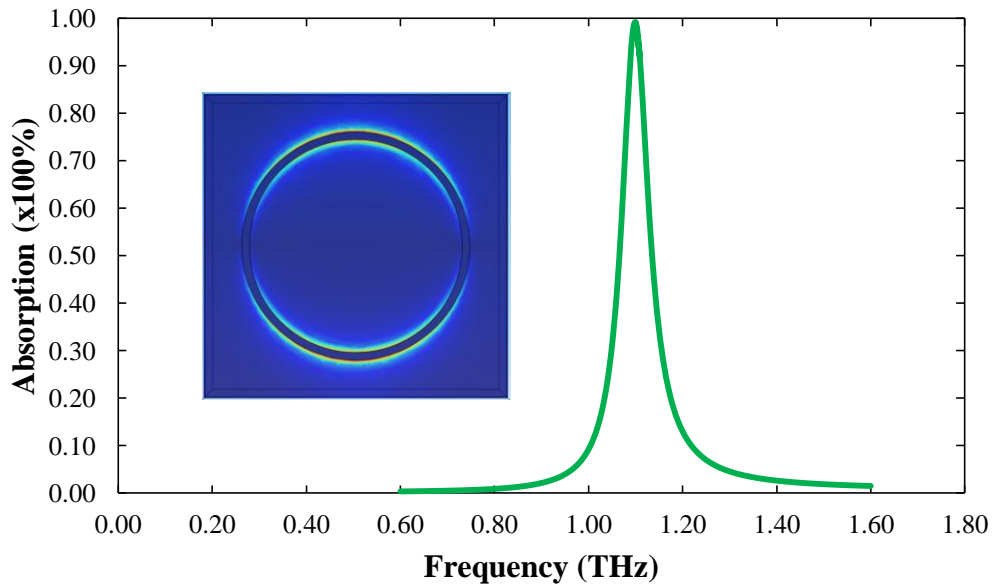
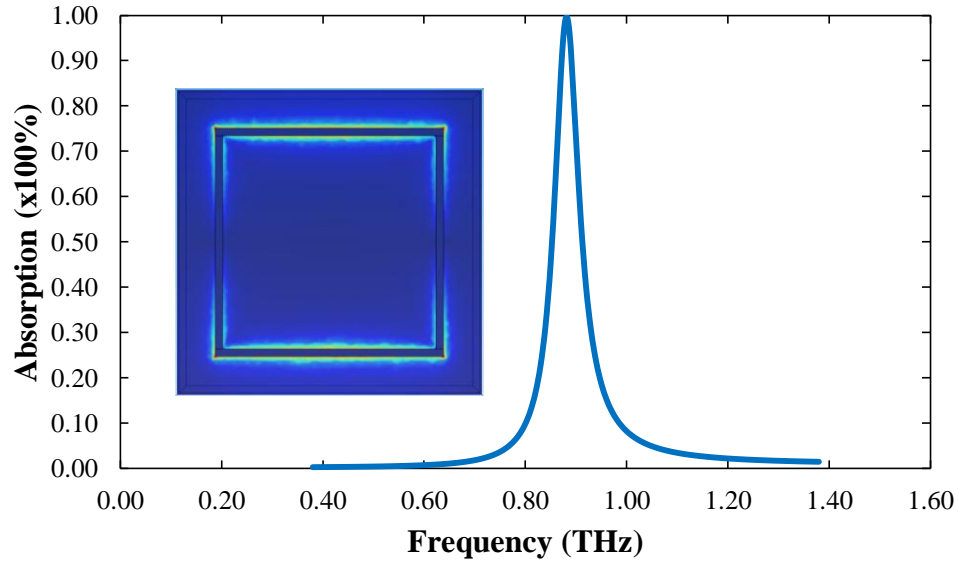


Figure 2.10 Absorption spectra of closed ring absorber structures with electric responses (inset) at resonance

Thus, these two designs exhibit absorptions of 99.6% (square) and 99.1% (circular). These near-unity absorptions occur at center frequencies 0.881 THz and 1.099 THz for the square-ring and circular-ring structures, respectively. It is of importance to note the behavior of surface current,

induced by the incident field, on these absorber structures. The surface current on each closed-ring absorber structure is shown in Figure 2.11.

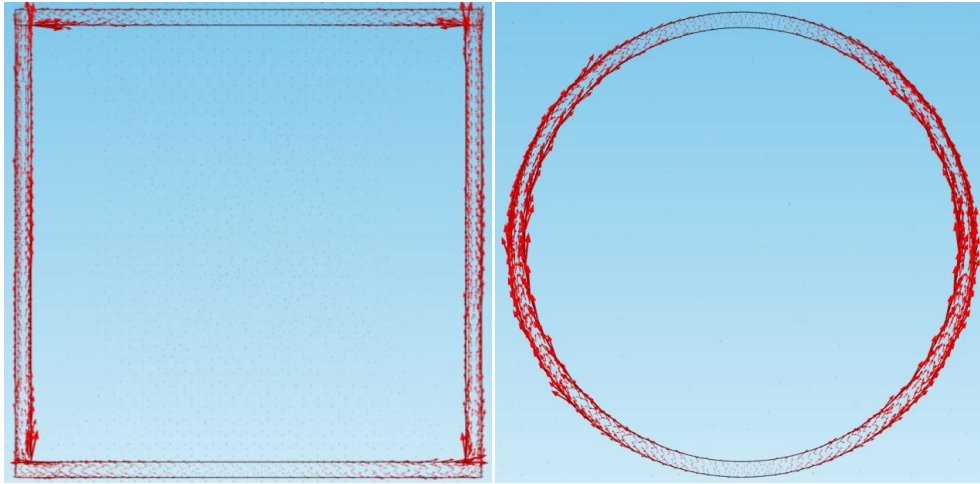


Figure 2.11 Surface current on the closed rings of square-ring (left) and circular-ring (right) absorbers

The red arrows in Figure 2.11 represent the surface current with the arrow size being proportional to current intensity. Note that the incident field induces surface current in opposite directions concentrated on the sides of the rings.

2.3.2 Proposed Design: Polarization-Insensitive THz Absorber

For implementation into applications it is highly desirable that absorber structures can operate using a wide range of incident field polarizations. This functionality improvement would allow an absorber to perform in a variety of environments and under a variety of conditions. To achieve this, we designed a metamaterial absorber structure similar to that of Figure 2.7 which consists of two additional interior “plates”. This new structure is shown in Figure 2.12.

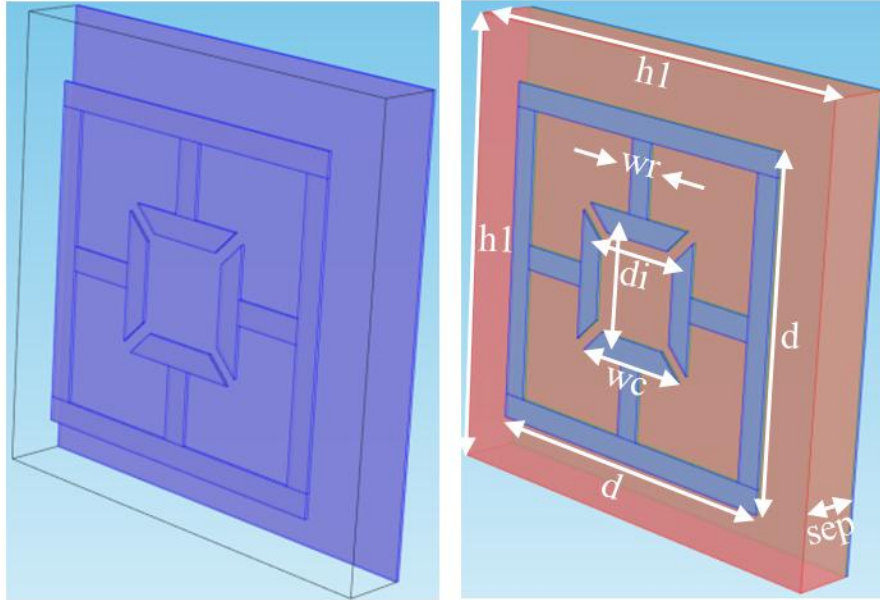


Figure 2.12 Polarization-insensitive THz metamaterial absorber structure

The configuration shown in Figure 2.12 is very similar to the design proposed by H. Tao et al in that it consists of two metallic layers with a dielectric spacing layer in between. Again, the back metallic layer is a continuous ground plane which prevents any transmission of electromagnetic radiation through the structure. Also, like the design of Figure 2.7 the top metallic layer of the new design in Figure 2.12 is an electric ring resonator (ERR). But the ERR in the design of Figure 2.12 contains four gaps, whereas the design of Figure 2.7 only contains one gap. Additionally, each ERR gap in the design of Figure 2.12 is arranged at equal distance and at 90° from each adjacent gap. For this reason, this design is proposed to be quite insensitive to incident field polarization. Since the primary electric response is generated by the gaps on the ERR, operation of the design of Figure 2.7 is strictly limited to incident field polarizations consistent with that shown in the figure. But since the new design shown in Figure 2.12 has four gaps on the ERR, it should be able to generate an electric response for a wide range of incident field polarizations. This feature would allow this configuration to have a significant operation

advantage over the earlier design shown in Figure 2.7 since it would not be limited to specific polarizations of incident radiation. Figure 2.13 and Figure 2.14 display tests which are very important to the efficient operation of absorbers.

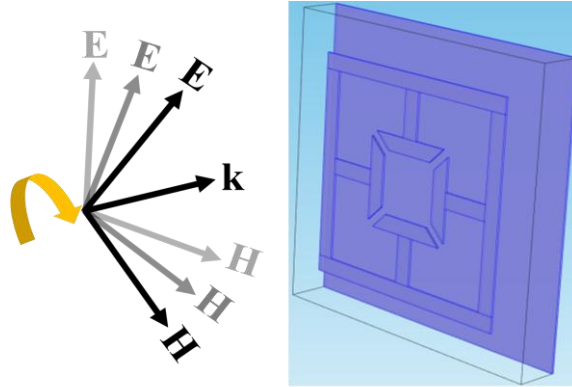


Figure 2.13 Various field polarization angles incident upon a THz metamaterial absorber

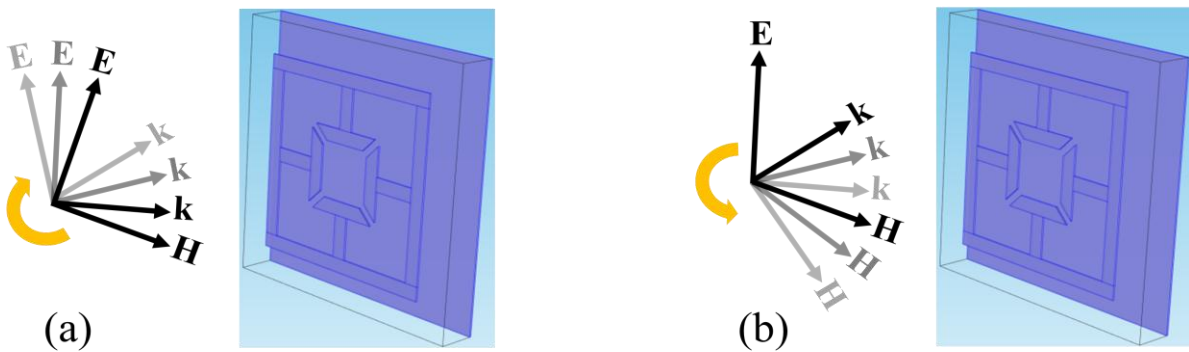


Figure 2.14 Rotations to test absorber sensitivity to various incidence angles (a) Rotations about magnetic field. (b) Rotations about electric field

Insensitivity to incident field polarization (Fig. 2.13) and insensitivity to angle of propagation (Fig. 2.14) are very important properties that metamaterial absorbers are desired to exhibit.

Efficient absorber performance under conditions of various polarization angles and angles of

propagation will allow an absorber structure to be very versatile. Such versatile absorbers could benefit many sensor/detector devices and interference reduction applications.

2.3.3 Broadband THz Absorber

For many applications, especially interference reduction applications, it may be desired that absorber structures operate over a wide range of frequencies. Since the mechanism that causes absorption in the aforementioned structure of Figure 2.9 is dipole resonances rather than LC resonances, the top rings may be arranged concentrically. One such concentric ring configuration under study in this work is shown in Figure 2.15.

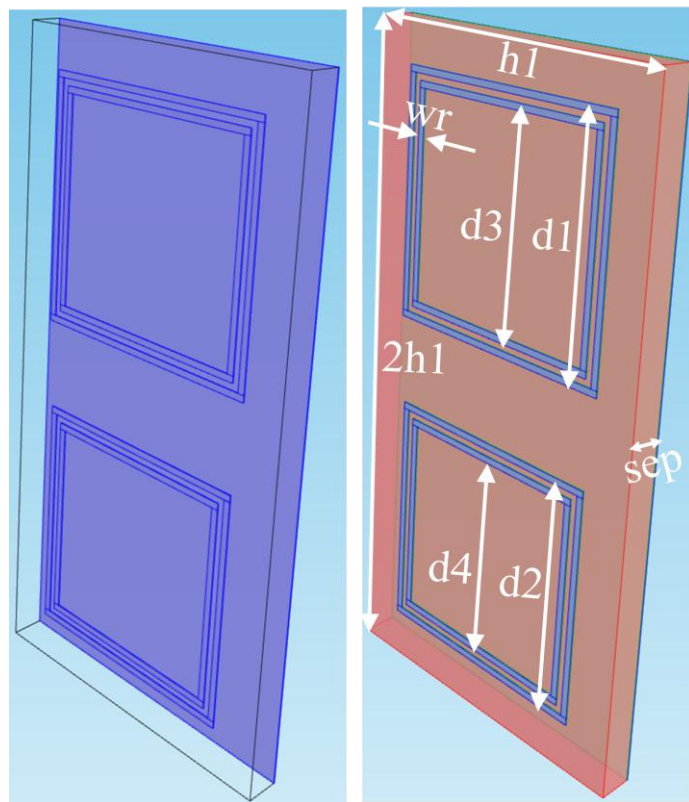


Figure 2.15 Designed structure for THz metamaterial broadband absorber

In addition to this square-ring design, another similar structure under study in this work is a broadband absorber utilizing circular closed rings. Having the same operating principle, this circular-ring structure is shown in Figure 2.16.

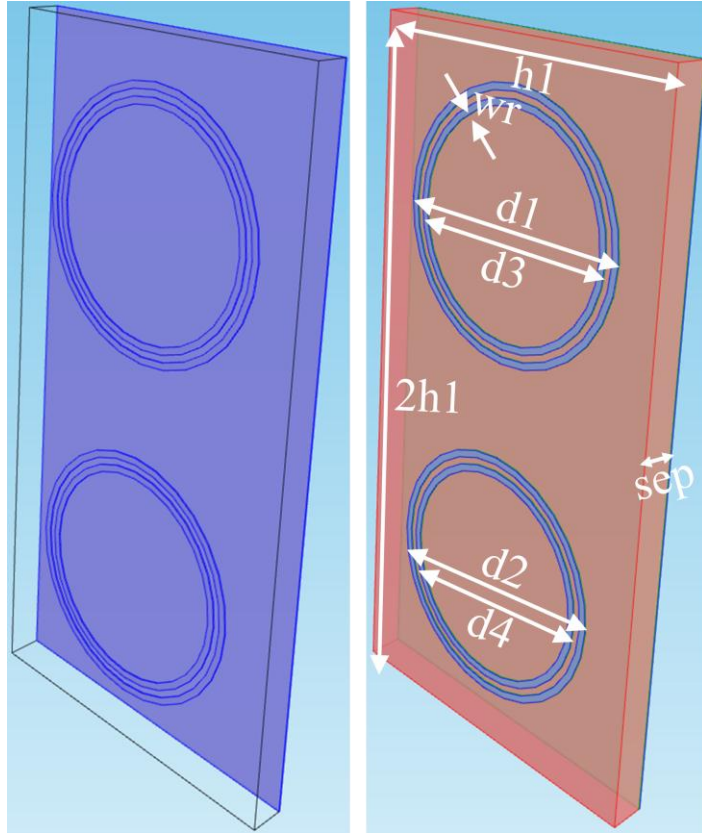


Figure 2.16 Circular ring design structure for THz metamaterial broadband absorber

Since the rings in these structures are closed, no coupling or interference between adjacent rings is expected. This property allows many rings to be arranged concentrically (with limitations) for the purpose of multiband and broadband absorbers. Additional closed-ring broadband absorber structures that contain more concentrically arranged rings have also been studied in this work. The rings on these structures were arranged as shown in order to provide the maximum absorption, which will become evident in Chapter 3.

CHAPTER 3

FEA SIMULATIONS

Simulation software was used to support the design and development of the metamaterial devices studied in this work. The software package chosen for this work was COMSOL Multiphysics [28]. This software makes use of the finite element method to approximate solutions for Maxwell's equations. Finite element analysis (FEA) software was selected due to its ability to model more complex geometries than other methods such as the finite difference method. Subsequent device fabrication was based on results from the simulated solutions.

3.1 Simulation Method

The finite element method was used to predict and confirm the behavior of metamaterial structures. This solving technique is a powerful method of approximating solutions to partial differential equations (PDE's). Finite element analysis (FEA) is capable of simulating the behavior of very complex structures. The finite element method was first used to solve mechanical deformation and stress problems. Eventually, FEA was adapted to approximate solutions to Maxwell's equations for electromagnetic fields analysis. First, the structure under study is constructed (3-dimensional). Boundary conditions are imposed on each domain of the structure based on the desired study. The finite element method then divides the structure into many smaller, simpler *elements* in a process known as meshing. The number of elements

produced can be adjusted to achieve the desired solution resolution (with limitations). Adjacent elements are connected at nodes as shown in Figure 3.1.

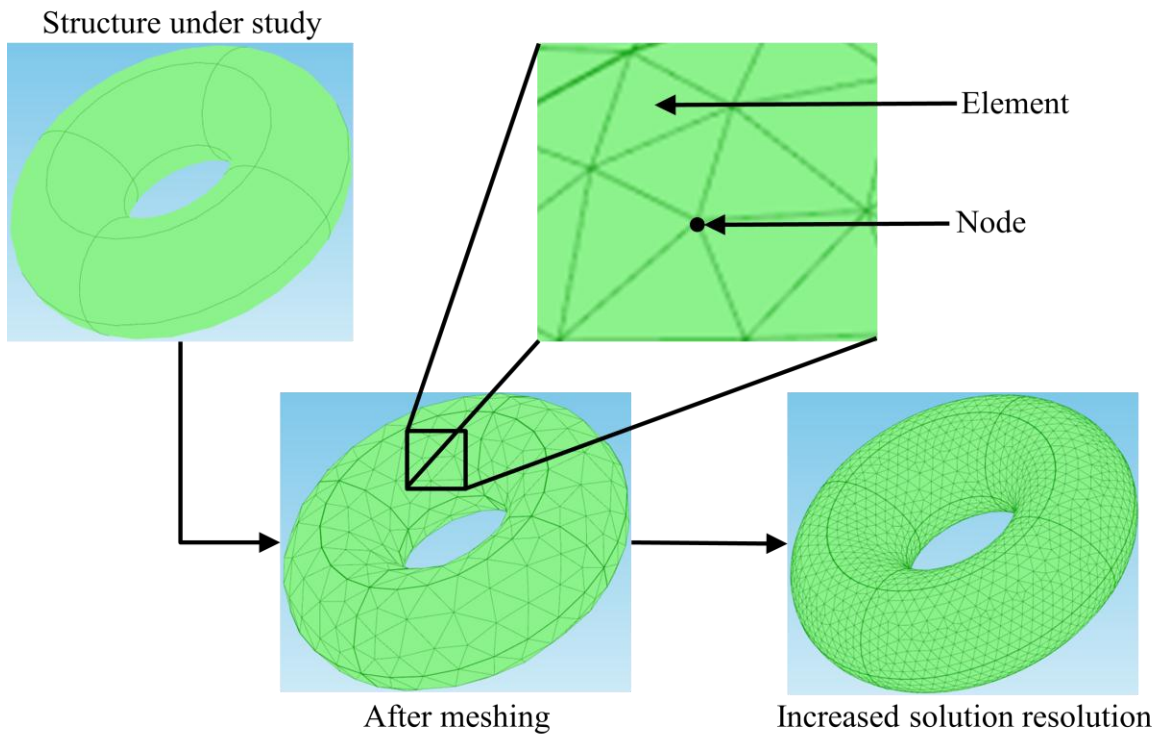


Figure 3.1 The finite element method process of meshing and refining

The desired field expressions to be approximated are interpolated by polynomials over each element. The result of this interpolation is a large set of algebraic equations to be solved simultaneously. The collection of elements and nodes results in a *finite* number of degrees-of-freedom (DOF) to be solved over, whereas continuous structures have an infinite number of DOF. Unknown field quantities over each element are found from the approximated solutions. The resulting approximated solutions can then be viewed for interpretation. Using the solutions, many other field quantities may also be calculated (power, energy, etc.).

3.2 Results

Finite element analysis simulations were carried out on all aforementioned absorber structures that we designed. Presented first are the simulation results for the structure of Figure 2.12 excited by a plane wave incident normal to the structure surface. Next, the simulation results are shown for various incident field polarization configurations on the structure of Figure 2.12. Shown last are the simulation results for the broadband absorber structures of Figure 2.15 and 2.16 excited by a plane wave at normal incidence.

3.2.1 Normal Incidence Tests

To prove matched performance with the design of Figure 2.7 at normal incidence, three variations on the design of Figure 2.12 have been modeled and simulated (X, Y, Z) using the finite element method. The two metallic layers (highlighted purple in Fig. 2.12) were modeled as copper with frequency independent conductivity $\sigma = 6 \times 10^7$ S/m. Each of the metallic layers was modeled 400 nm thick. The dielectric layer between metallic layers (highlighted red in Fig. 2.12) was modeled as polyimide with $\sigma = 6.7 \times 10^{-16}$ S/m, $\epsilon = 3.0 + i0.03$, and $\mu = 1$. The real component of the dielectric permittivity was obtained through experimental reflectance measurements and the imaginary component was found experimentally using ellipsometry. The absorber of Figure 2.12 was modeled in a free-space medium as the unit cell of an infinite array of absorbers in both directions along the plane perpendicular to the direction of propagation. Table 3.1 displays geometrical parameters for the three simulated absorbers of Figure 2.12.

Table 3.1 Geometrical parameters for proposed polarization-insensitive absorber

Design	Geometrical Parameters						
	d (μm)	d_i (μm)	w_r (μm)	w_p (μm)	h_1 (μm)	<i>Metallic Layer Thickness</i> (μm)	sep (μm)
X	56	20	4	21	75	0.4	9.4
Y	50	18	3.5	19	67	0.4	8.5
Z	44	15.5	3	16.5	59	0.4	7.1

The values displayed in Table 3.1 have been found to provide maximum absorption at normal incidence. The simulated absorption spectrum for each variation on the design Figure 2.12 is shown in Figure 3.2. Since this structure provides $T(\omega) = 0$, the absorption (or absorbance) can be calculated simply by

$$A(\omega) = 1 - R(\omega) \quad (3.1)$$

Reflection, $R(\omega)$, is defined to be

$$R(\omega) = \frac{(\text{Power Incident on Structure}) - (\text{Time-Average Power Delivered to Structure})}{\text{Power Incident on Structure}} \quad (3.2)$$

The electric (inset top) and magnetic (inset bottom) responses at resonance are also shown in Figure 3.2.

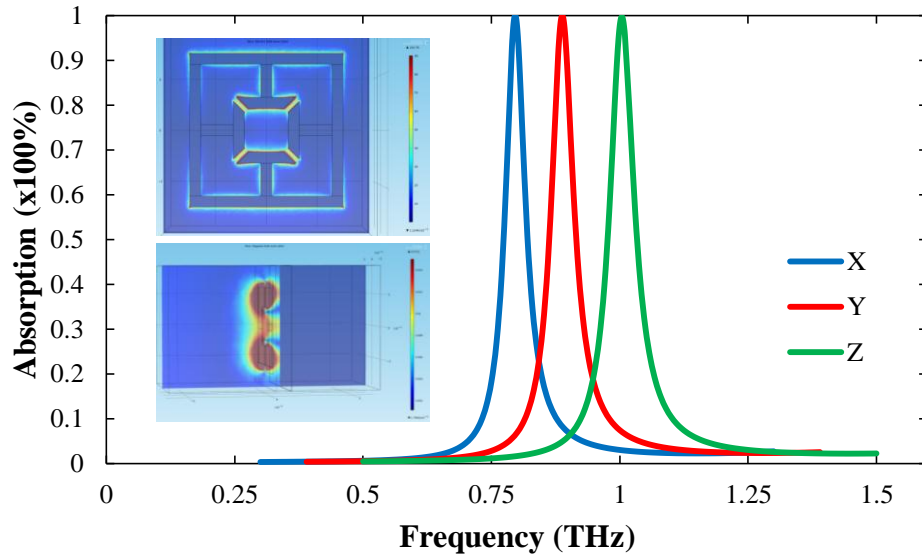


Figure 3.2 Absorption spectra with electric response at resonance (inset top) and magnetic response at resonance (inset bottom)

Thus, designs X, Y, and Z exhibit absorptions of 99.9%, 99.9%, and 99.7%, respectively. These near-unity absorptions occur at center frequencies 0.796 THz, 0.888 THz, and 1.004 THz for designs X, Y, and Z, respectively. These absorption peaks offer a FWHM from 0.045 THz to 0.06 THz making this absorber structure even more attractive for spectrally-selective imaging applications than the design of Figure 2.7.

In order to optimize these structures to obtain such high absorptions as shown in Figure 3.2, the exact parameters must be found that provide a match of permittivity and permeability which in turn provides an impedance match to free-space. The parameter most sensitive to absorption levels is the spacing distance between metallic layers (dielectric layer thickness). A simulated sweep on this spacing (called *sep* here) was performed for each of the variations on the design of Figure 2.12. The results from design Y are shown in Figure 3.3 revealing a glimpse of the sensitivity of these structures to dielectric spacer thickness.

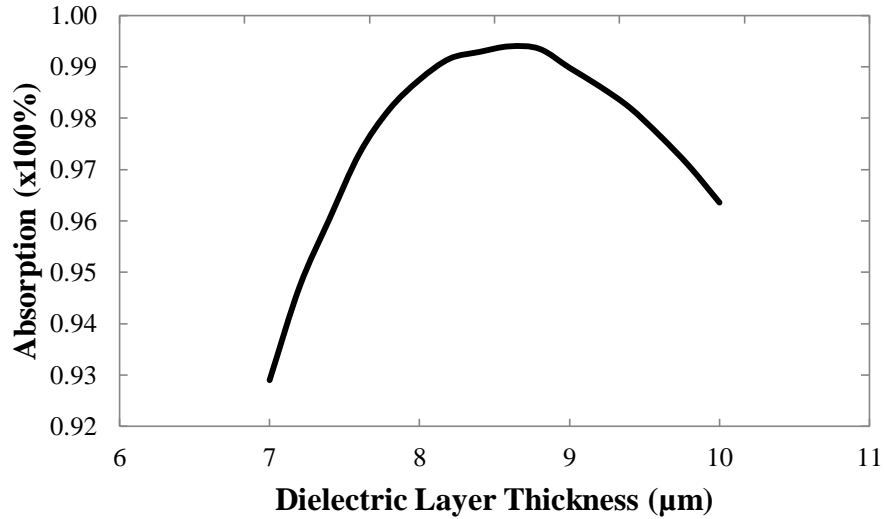


Figure 3.3 Effect of dielectric layer thickness variation on absorption

At resonance frequency, there is very little reflection ($< 1\%$) from the metamaterial absorber structure which causes such high absorption. But according to conservation of energy, the power incident on the structure must reside somewhere. The energy is mostly stored in the dielectric spacing layer and the ERR. It is possible that a very small amount will be converted to heat. To get a good visual understanding of the field behavior in the absorber, we can take a look at the electric field intensity. Figure 3.4 shows a single cross-section of the magnitude of the electric field as well as the magnitude of the magnetic field at a non-resonance frequency and the same cross-section at resonance frequency. Only the results from design Y is shown here but the results of designs X and Z are very similar.

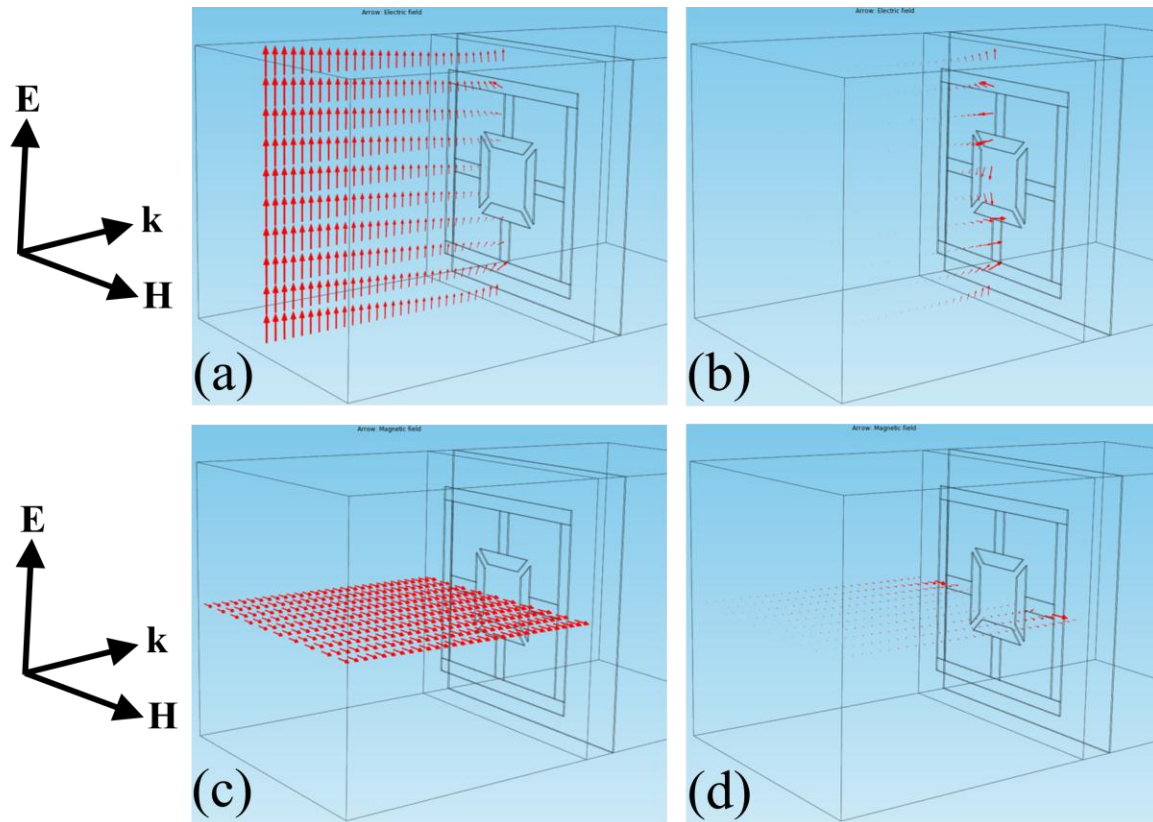


Figure 3.4 Electric and magnetic field vectors which were solved using FEA at normal incidence. Electric (a) and magnetic (c) field vectors at non-resonance frequency (0.4 THz). Electric (b) and magnetic (d) field vectors at resonance frequency (0.888 THz)

The red arrows in Figure 3.4 represent the scattered electric or magnetic field intensity. At non-resonance frequency, the solution results in a large amount of reflection ($> 99\%$) which is visible by the high density of red arrows in Figure 3.4 (a) and (c). But at resonance frequency, the solution reveals that the reflected electric field and magnetic field (and thus reflected power) are extremely small ($< 1\%$) which is visible by the lack of red arrows in Figure 3.4 (b) and (d).

3.2.2 Polarization Sensitivity Tests

One important feature of the design of Figure 2.12 is that it is proposed to be insensitive to incident field polarization. To test this hypothesis, finite element simulations were carried out

for two additional polarization angles (15° and 45°). The rotation angles of polarization were performed as shown in Figure 2.13. The particular simulations used to test polarization angles were performed using the optimized structure of design Y. To test polarization insensitivity, only three angles of incident polarization were simulated. But due to both vertical and horizontal symmetry, any subsequent polarization rotation of 90° will result in the same solution and thus, the same absorption spectrum. This property is in stark contrast to the design of Figure 2.12 which would result in an extremely low absorption upon rotation of 90° from the incident field polarization shown in Figure 2.7. Figure 3.5 shows a comparison of the absorption spectra resulting from the two additional polarization angles.

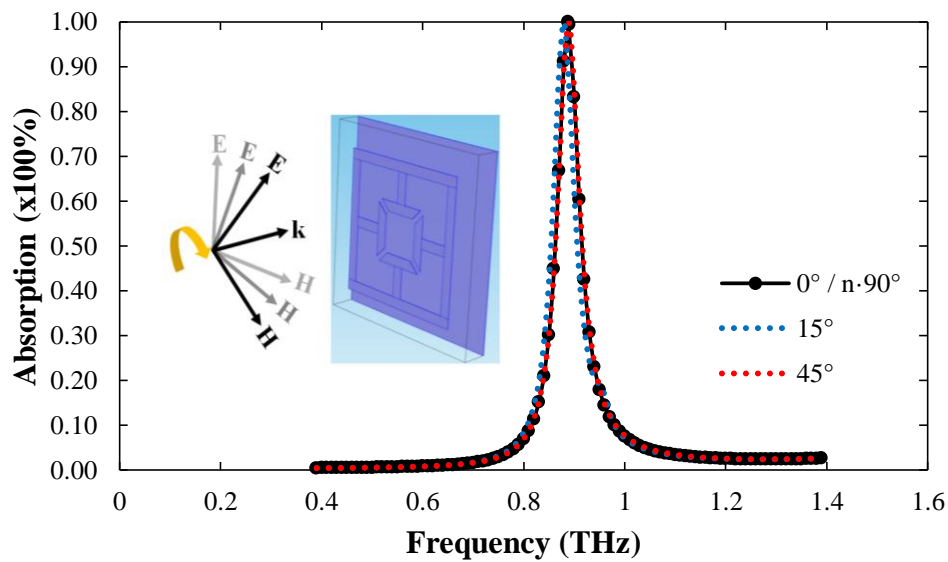
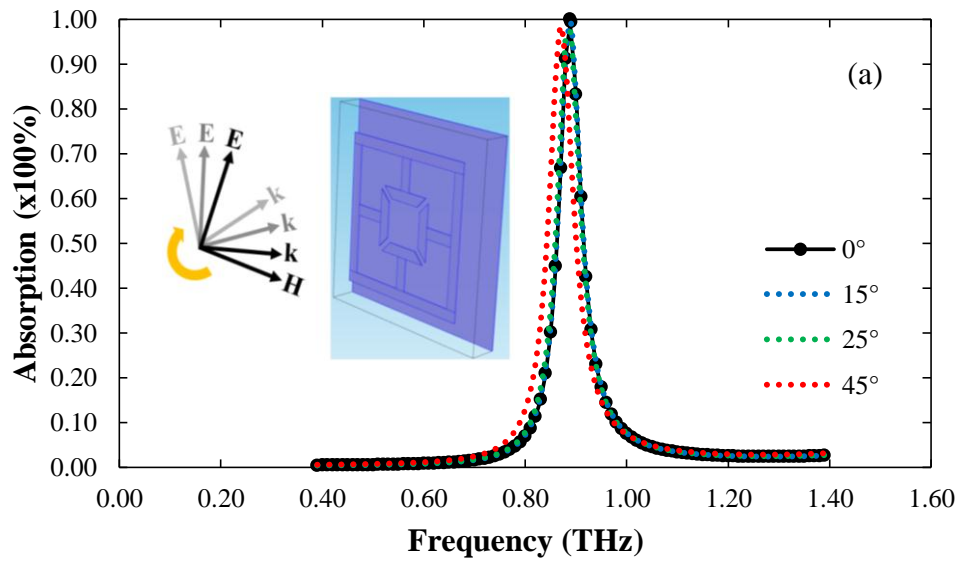


Figure 3.5 Absorption spectra resulting from variance in polarization angles

Demonstrating the versatility of this absorber structure, these polarization angles each result in absorptions greater than 99%. This finding confirms that the design of Figure 2.12 would be ideal for applications in spectrally selective imaging as well as applications to reduce interference. But these simulations were all performed with the incident radiation at normal

incidence (0°). To further test the insensitivity of the design of Figure 2.12 to incident radiation, computer simulations were performed on design Y for various radiation oblique incidence angles. To ensure a robust testing procedure, the structure was tested for incidence angles relative to the electric field polarization as well as relative to the magnetic field polarization as shown in Figure 2.14. Simulations were carried out on design Y for three additional incidence angles (15° , 25° , and 45°) relative to the electric field as well as the magnetic field. Figure 3.6 shows a comparison of the absorption spectra resulting from the three additional incidence angles for each case.



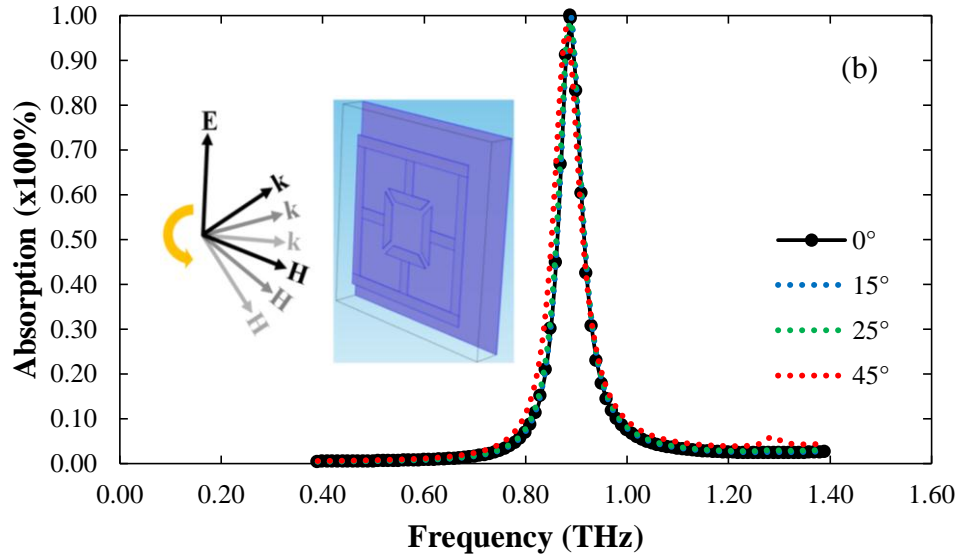


Figure 3.6 Absorption spectra resulting from various incidence angles. (a) From rotations about incident electric field and (b) from rotations about incident magnetic field

Incidence angles varied in both directions result in absorptions $> 96\%$ for all tested angles which allows this design to be an excellent candidate for applications in interference reduction as well as spectrally selective imaging. Despite a very slight frequency shift for 45° about the electric field, according to simulations the design of Figure 2.12 is able to obtain high absorption (near unity) for a wide range of incidence angles. In addition to polarization and incidence angle insensitivity, the design of Figure 2.12 has distinct important advantages over other absorber designs. This design is very thin ($6\text{-}9\ \mu\text{m}$) and any substrate can be selected since the continuous ground plane provides zero transmission. Also, it is mechanically flexible allowing it to bend and wrap around objects which could likely be required in many applications.

3.2.3 Broad Band Absorption Tests

In order to develop an optimized design and demonstrate the performance of broadband absorbers, the designs of Figure 2.15 and Figure 2.16 have been modeled and simulated using

FEA. The two metallic layers (highlighted purple in Fig. 2.15 and Fig. 2.16) were modeled as copper with conductivity $\sigma = 6 \times 10^7$ S/m. Again, each of the metallic layers was modeled 400nm thick. The dielectric layer between metallic layers (highlighted red in Fig. 2.15 and Fig. 2.16) was modeled as polyimide with $\sigma = 6.7 \times 10^{-16}$ S/m, $\epsilon = 3.0 + i0.03$, and $\mu = 1$. The absorber structures were modeled in a free-space medium as described before. Table 3.2 displays geometrical parameters for the simulated broad band absorbers of Figure 2.15 and Figure 2.16.

Table 3.2 Geometrical parameters for proposed broadband absorbers

Geometrical Parameters						
$d1$ (μm)	$d2$ (μm)	$d3$ (μm)	$d4$ (μm)	wr (μm)	$h1$ (μm)	<i>Metallic Layer Thickness</i> (μm)
75	71	67	63	2	100	0.4

The simulated absorption spectra are shown in Figure 3.7 for various dielectric layer thicknesses (*sep*). Again, due to the presence of a ground plane, there is no transmission through the structure at THz frequencies so equations (3.1) and (3.2) are used to calculate absorption.

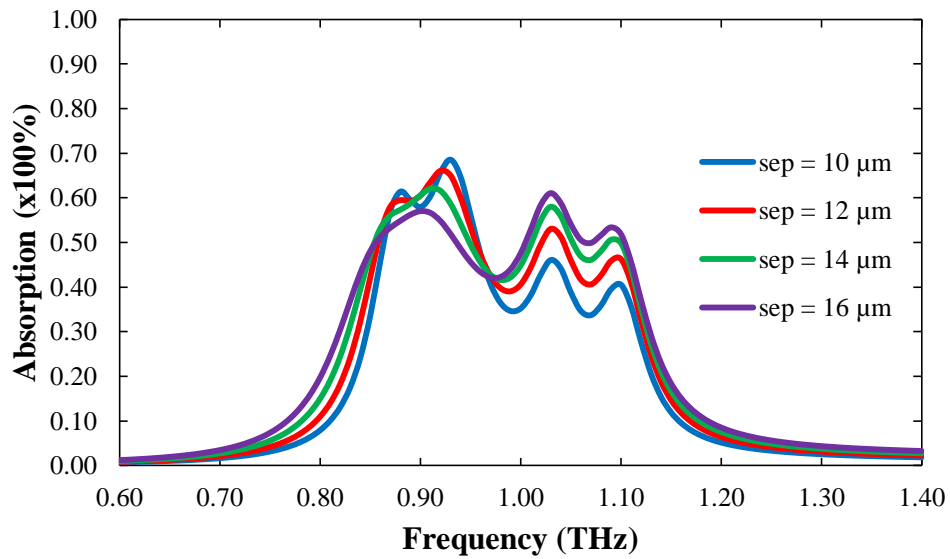
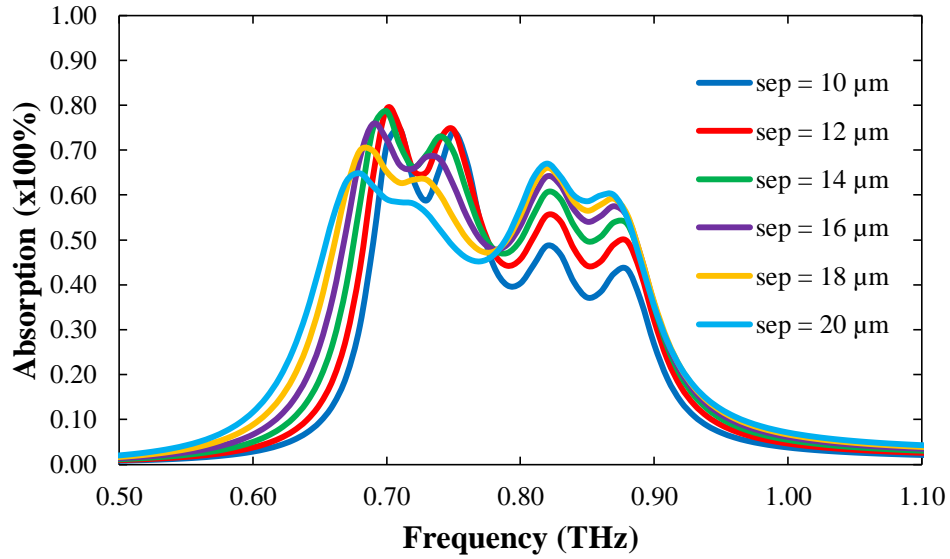


Figure 3.7 Absorption spectra of square-ring (top) and circular-ring (bottom) broad band absorbers

Thus, each of these broadband absorber designs result in a desirable wide FWHM. The square-ring design (top of Fig. 3.7) produces an absorption band of ~ 0.35 THz with an average absorption value of over 56% in this range. The various absorption spectra for this design also reveal that the dielectric thickness (*sep*) which provides optimum absorption was found to be 18

μm . The circular-ring design (bottom of Fig. 3.7) produces an absorption band of ~ 0.3 THz with an average absorption level of over 49% in this range. Additionally, the various absorption spectra for this design shows that the dielectric thickness (*sep*) which provides optimum absorption was found to be $14 \mu\text{m}$. The performance of each design is desirable for use in many applications, especially interference reduction applications.

Additional broadband absorber structures, very similar to those of Figure 2.15 and Figure 2.16, were designed and developed with the intention to increase the absorption band width. These additional structures (Figure 3.8 and Figure 3.9) contain eight closed rings, both square and circular, as opposed to four rings as in the previous designs.

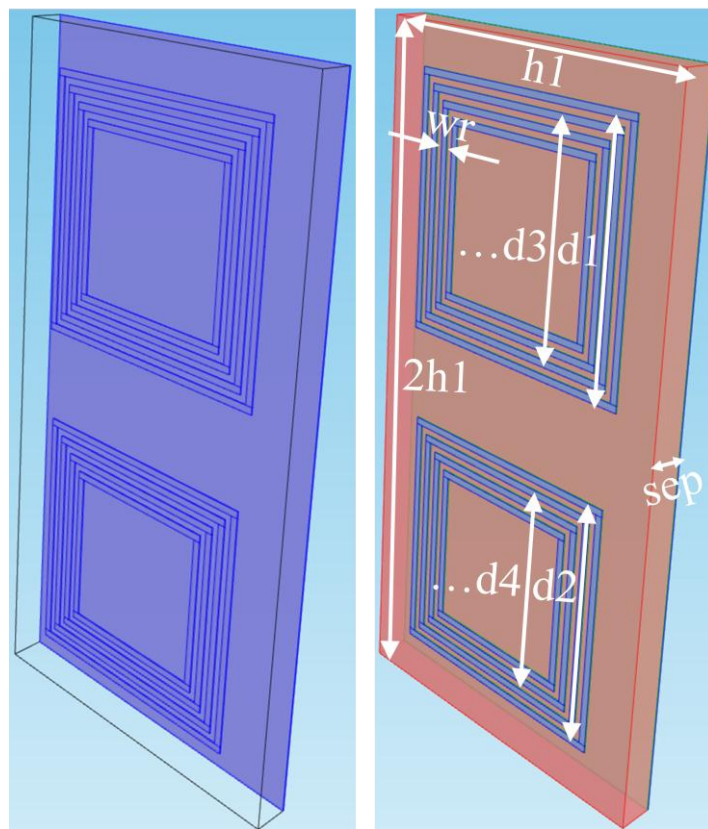


Figure 3.8 Square eight-ring broadband absorber structure

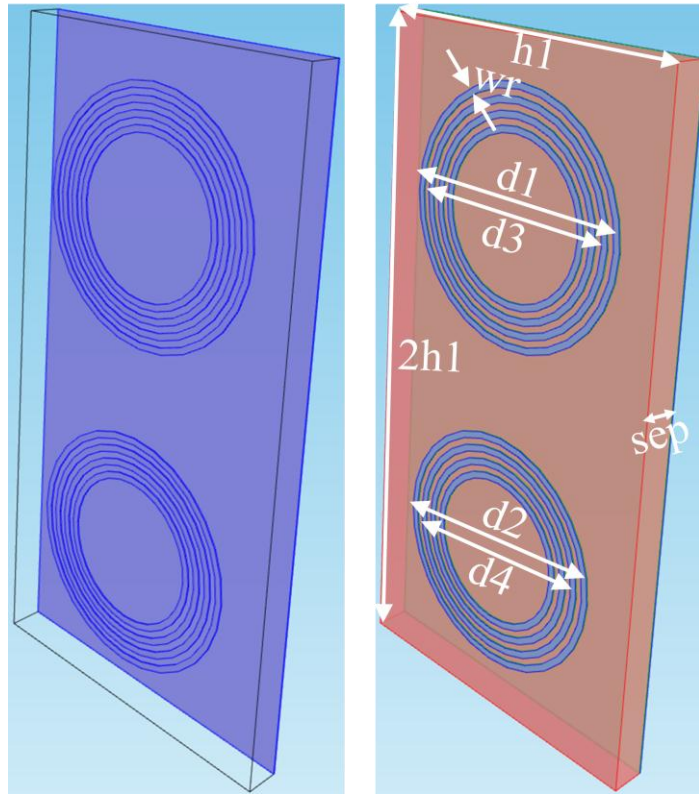


Figure 3.9 Circular eight-ring broadband absorber structure

Again, finite element simulations were first carried out on these structures to study the electromagnetic response and optimize the performance of the absorber configurations. Table 3.3 shows the geometrical parameters of the eight-ring structures. The naming convention for the geometrical parameters is consistent with that shown in Figure 2.15 and Figure 2.16.

Table 3.3 Geometrical parameters for proposed eight-ring broadband absorbers

Geometrical Parameters										
<i>d1</i> (μm)	<i>d2</i> (μm)	<i>d3</i> (μm)	<i>d4</i> (μm)	<i>d5</i> (μm)	<i>d6</i> (μm)	<i>d7</i> (μm)	<i>d8</i> (μm)	<i>wr</i> (μm)	<i>h1</i> (μm)	<i>Metallic Layer Thickness</i> (μm)
75	71	67	63	59	55	51	47	2	100	0.4

The simulated absorption spectra for the eight-ring structures are shown in Figure 3.10 for various dielectric layer thicknesses (*sep*). Once again, equations (3.1) and (3.2) are used to calculate absorption.

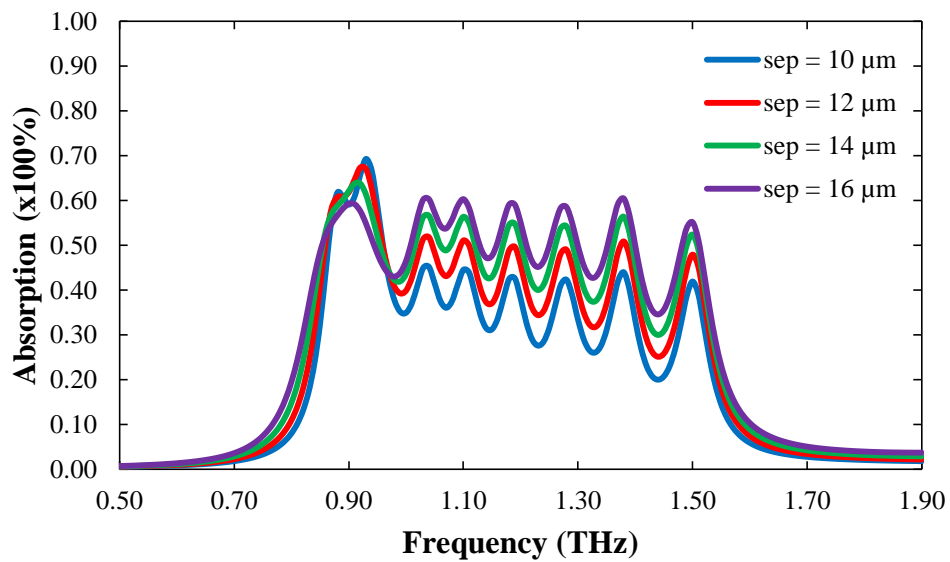
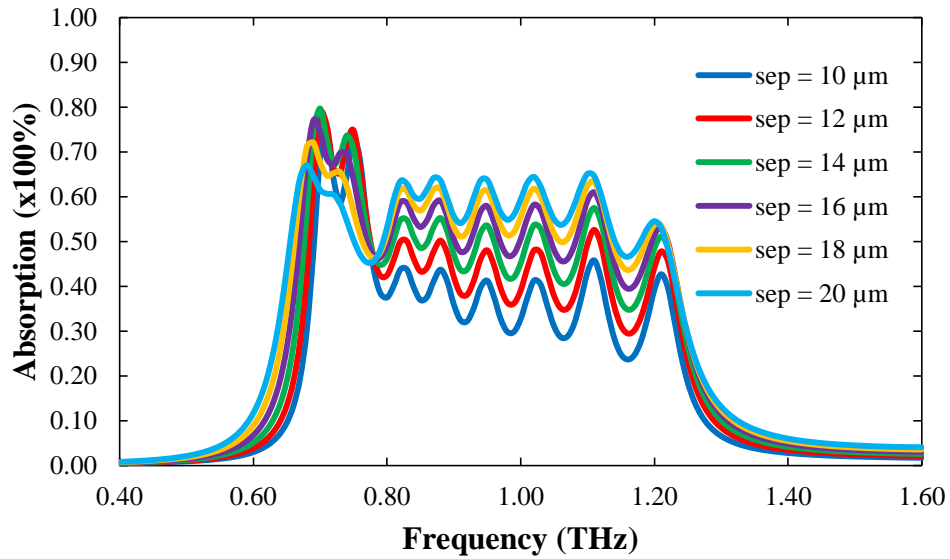


Figure 3.10 Absorption spectra of square-ring (top) and circular-ring (bottom) eight-ring broadband absorbers

Thus, each of the eight-ring broadband absorber designs result in a very desirable FWHM. The square-ring design (top of Fig. 3.10) produces an absorption band of ~ 0.6 THz with an average absorption value of $\sim 56\%$ in this range. The various absorption spectra for this design

demonstrates that the dielectric thickness (*sep*) which provides optimum absorption was found to be 20 μm . The circular-ring design (bottom of Fig. 3.10) produces an absorption band of ~ 0.71 THz with an average absorption level of over 50% in this range. Also, the various absorption spectra for this design shows that the dielectric thickness (*sep*) which provides optimum absorption was found to be 16 μm . Additionally, the performance of each eight-ring design is even more desirable for use in applications than the previous four-ring design due to wider absorption bands without compromising the absorption levels. Of course, however, both four-ring and eight-ring broadband absorbers have advantages and disadvantages which must be accounted for when implementing these devices into applications. For instance, some applications may not require absorption bands as wide as those provided by the eight-ring designs. In such a case, the four-ring absorbers may be more desirable due to more ease of fabrication. Furthermore, the work with these particular broadband absorbers suggests that the addition of more concentric closed rings, with limitations, would increase the width of the absorption band.

CHAPTER 4

EXPERIMENTAL MEASUREMENTS

Metamaterial THz absorbers have been fabricated based on the finite element simulation data obtained and displayed in the previous chapter. Absorbers structures were fabricated using the geometrical parameters which were found, through simulations, to provide the optimum absorption. The fabricated absorber arrays were then tested experimentally. In this chapter, the fabrication process as well as the experimental measurement technique is described. Lastly, results from the experimental measurements are presented and discussed.

4.1 Device Fabrication

The metamaterial absorber arrays were fabricated using typical photolithographic and electron beam evaporation techniques. First, using electron beam deposition a copper ground plane of appropriate thickness was evaporated onto a 250 μm -thick silicon wafer. A polyimide separation layer of appropriate thickness (found using simulation data) was then spun onto the ground plane. A diagram showing the absorber fabrication process is shown in Figure 4.1.

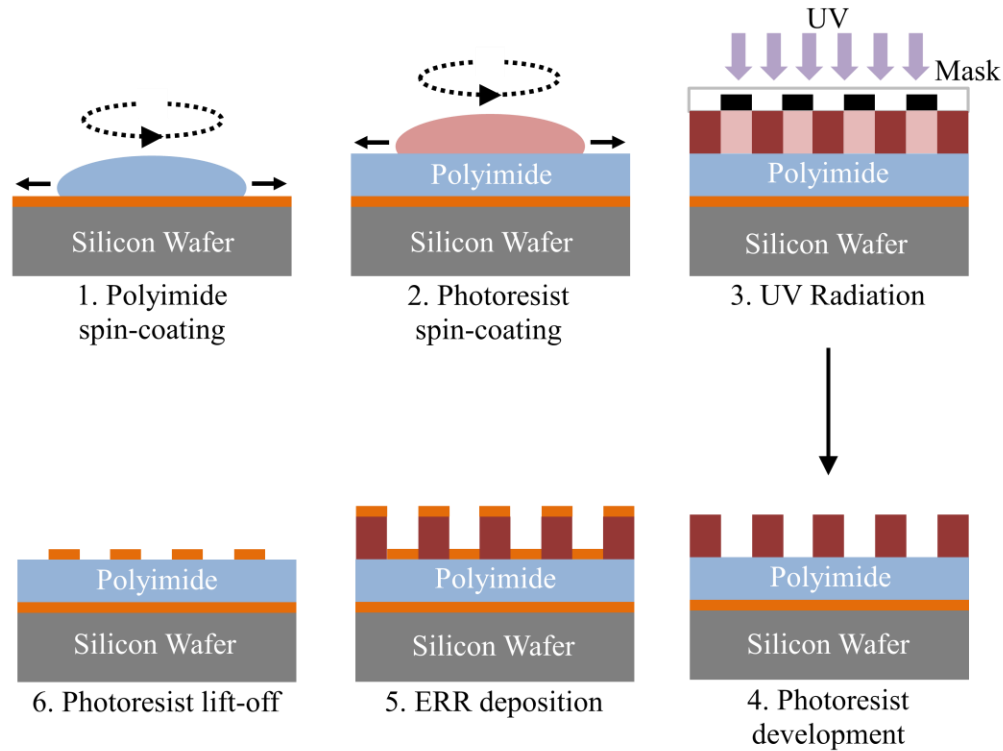


Figure 4.1 Metamaterial absorber fabrication process

The resulting structure was subsequently cured in a vacuum oven. Next, a $\sim 0.8 \mu\text{m}$ -thick layer of positive photoresist was spun on top of the polyimide layer. This photoresist layer was then soft-baked. A photomask containing the ERR or closed-ring designs was then aligned over the soft-baked wafer. Next, the masked configuration was briefly exposed to ultraviolet radiation. The ERR patterns were then able to be developed, clearing away the exposed photoresist. Again using electron beam evaporation, a layer of appropriately thick copper was evaporated onto the structure to form the ERR array. Finally, the structure was sonicated in acetone in order to remove the remaining photoresist. Optical microscope images of the fabricated ERR arrays are shown in Figure 4.2.

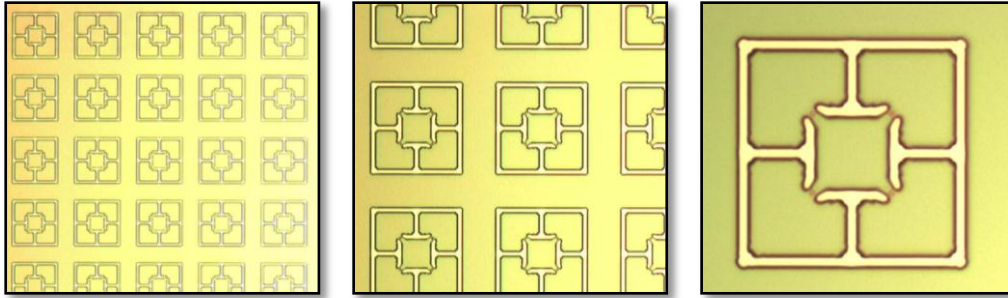


Figure 4.2 Optical microscope images of fabricated metamaterial absorber array

4.2 Measurement Technique

The objective of carrying out experimental measurements on the fabricated absorbers was to obtain absorption spectra in order to observe device performance. The absorber structures under study in this work have metallic ground planes which prevent any transmitted THz waves through the structures. Thus, in order to calculate absorption in accordance with (3.1) and (3.2), only incident and reflected powers are required to be measured. Reflection from the absorber structures was measured using a THz time domain spectrometer. The spectrometer was pumped with a titanium-sapphire LASER which emits 120 femtosecond pulses at a 775 nm wavelength. THz waves are produced in the spectrometer using a high-voltage biased photoconductive antenna. The THz pulses are detected using the electro-optic sampling technique. An off-axis parabolic mirror was used to focus the THz beam onto the absorber arrays. The THz beam reflected from the absorber structures was then re-collimated using another parabolic mirror prior to finally reaching the detection array. A diagram of the experimental measurement setup is shown in Figure 4.3.

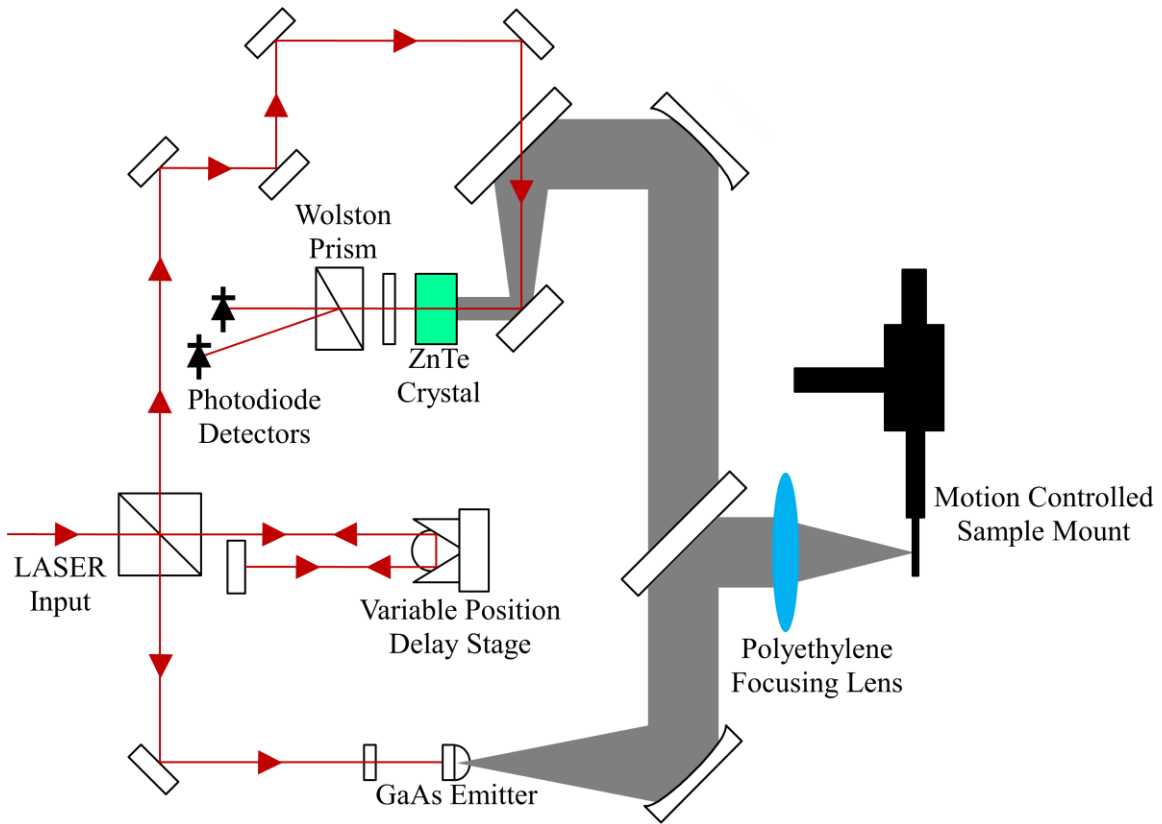


Figure 4.3 Experimental setup for study of metamaterial absorbers

4.3 Results

Experimental measurements, using a reflection-mode time domain spectrometer, were carried out on several selected fabricated absorber arrays. First presented are some absorption spectra from both aforementioned narrow-band absorber designs (Fig. 2.7 and Fig. 2.12), which demonstrate operability. Shown next are absorption spectra resulting from geometrical variations on the absorber structure of Figure 2.12. Presented last are absorption spectra displaying the effect of incident field polarization configurations on the absorber design of Figure 2.12.

4.3.1 Normal Incidence Tests

To demonstrate the performance of the fabricated absorber arrays, experimental measurements were carried out with slight modifications on the previously mentioned absorber designs. These modified designs are denoted by B', Y', and Z'. It is important to note that due to deposition limitations, the metallic layers of the fabricated absorber arrays are 200 nm thick. Also due to fabrication limitations, the polyimide layer deposited to produce the following results was 3.5 μm thick. The geometrical parameters of these fabricated absorber devices are displayed in Table 4.1.

Table 4.1 Geometrical parameters for fabricated absorber arrays

Geometrical Parameters							
<i>Design of Figure 2.7</i>							
Design	d (μm)	w_r (μm)	w_c (μm)	g (μm)	h_1 (μm)	<i>Metallic Layer Thickness</i> (μm)	sep (μm)
B'	30	3	11	2	40	0.2	3.5
<i>Design of Figure 2.12</i>							
Design	d (μm)	d_i (μm)	w_r (μm)	w_p (μm)	h_1 (μm)	<i>Metallic Layer Thickness</i> (μm)	sep (μm)
Y'	50	18	3.5	13	67	0.2	3.5
Z'	44	15.5	3	10	59	0.2	3.5

The experimental absorption spectra for the fabricated absorber arrays are shown in Figure 4.4. The experimental spectra are plotted together with the simulated spectra obtained from finite element analysis.

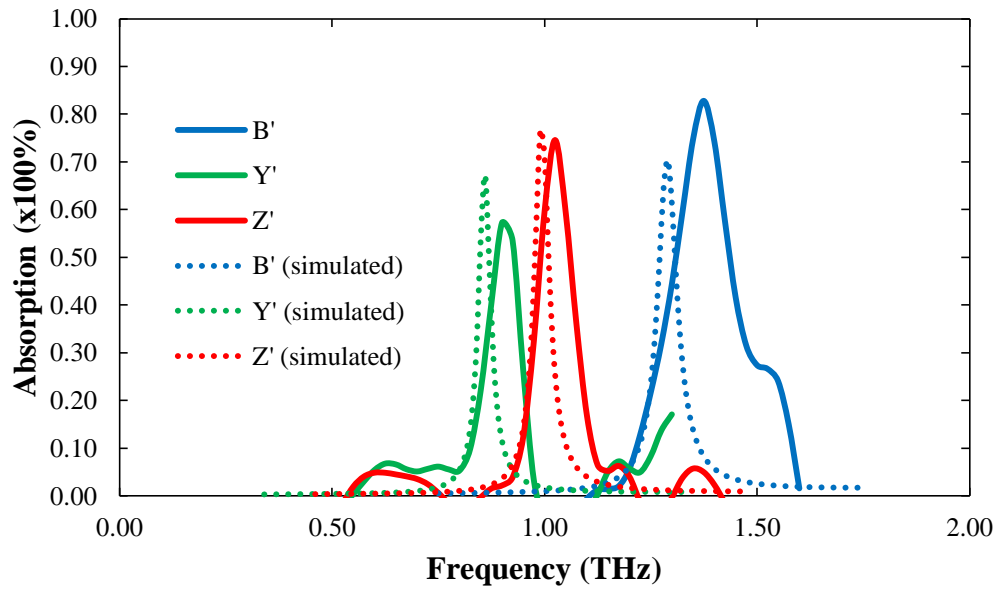


Figure 4.4 Experimental absorption spectra of fabricated absorber arrays

Notice that the measured spectra closely match that of the simulated spectra, having only a slight discrepancy of resonance frequency. In this case the simulated absorbers were modeled with polyimide permittivity $\epsilon = 3.5 + i0.03$. Figure 4.5 shows that this discrepancy may be corrected by modeling the polyimide layer with permittivity $\epsilon = 3.0 + i0.03$.

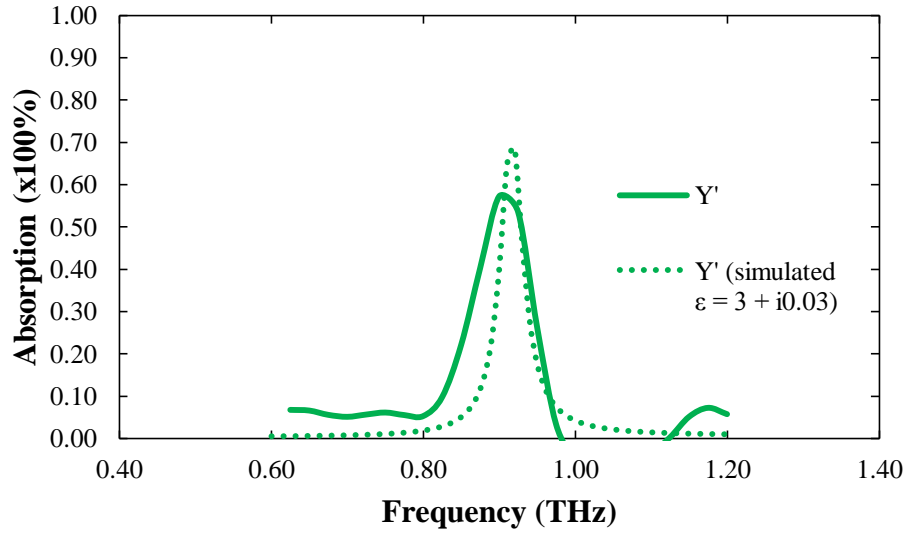


Figure 4.5 Absorption spectrum of Y' showing discrepancy correction

This result is precisely the reason that all previous simulations modeled the polyimide spacer layer with $\epsilon = 3.0 + i0.03$. Together, the results of Figure 4.4 and Figure 4.5 demonstrate that the fabricated absorber arrays are indeed highly absorbent and spectrally selective, having absorptions near the expected levels and very near the anticipated frequencies of simulated models. Thus, the fabricated devices show strong potential for use in many detector/sensor applications. It is expected that these devices would achieve near-unity absorption if they were fabricated with the optimum geometrical parameters.

4.3.2 Polarization Sensitivity Tests

Experimental measurements were also performed on a selected array of the fabricated absorbers in order to test the important property of polarization sensitivity. This test was performed by rotating the absorber array, about its center, relative to the incident field polarization at three angles (0° , 15° , and 45°). The polarization variations were tested on a modification on design Y, with $sep = 20 \mu m$. The absorption spectra resulting from these

experimental measurements are shown in Figure 4.6 which also indicates normal incidence polarization configuration and subsequent rotation.

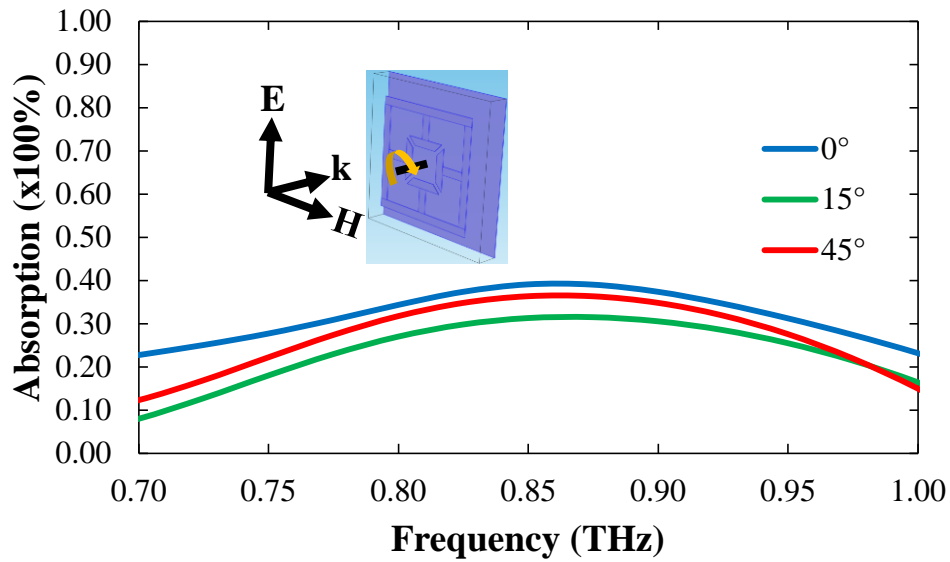


Figure 4.6 Absorption spectra resulting from experimental measurements of polarization variations

Although the absorption is seen to decrease upon varying the incident field polarization configuration, the amount is very small so the absorber still operates at acceptable levels and at the same resonance frequency. Again, the device could demonstrate less discrepancy from simulation if the fabricated absorber geometrical parameters were more closely matched. Even though the absorber device did not perform near perfection as anticipated, the performance and versatility does show promise for use in many detector/sensor applications.

CHAPTER 5

CONCLUSIONS AND FUTURE WORK

5.1 Summary

In this work, metamaterial absorber devices have been designed, simulated, fabricated, and characterized. The structure of Figure 2.12 was designed to be thin, flexible, and insensitive to incident field polarization and propagation angle. Finite element analysis simulations were used to optimize the absorption and confirm that the device is highly insensitive to incident field polarization and angle of propagation. Absorber devices were fabricated using standard photolithography and electron beam deposition techniques. Although experimental measurements did not produce ideal results, the obtained results demonstrated the operability and versatility of the device. The structures of Figure 2.15 and Figure 2.16 were designed to produce broad absorption spectra. Finite element analysis simulations were also performed on these structures to optimize absorption strength and spectra width. The simulated solutions show that these broadband absorbers indeed produce broad absorption spectra, but at the cost of absorption strength.

5.2 Future Work

This work leaves much room for improvement upon metamaterial absorbers. The development, fabrication, and characterization presented here have laid a solid foundation to build upon. Many detector/sensor applications exist for which metamaterial absorbers would

improve. For example, it is agreed by many researchers that narrow-band metamaterial absorber devices show potential for use as fundamental detection elements in imaging applications. Improvement upon the groundwork performed in this study could significantly benefit the practicality of such applications. Also, broadband absorber devices show strong potential to be used in interference reduction applications to neglect unwanted frequencies. Increasing spectra width and absorption, although seemingly difficult, would certainly enhance the usefulness of such devices and provide great applicability. Any advancements in the metamaterial absorbers presented in this work could potentially benefit many scientific areas including chemistry, biology, security, and medicine.

REFERENCES

- [1] J.B. Pendry “Negative Refraction Makes a Perfect Lens”, *Physical Review Letters*, vol. 85, no. 18, pp. 3966-3969, 2000
- [2] J.B. Pendry, D. Schurig, D.R. Smith, “Controlling Electromagnetic Fields”, *Science*, vol. 312, iss. 5781, pp. 1780-1782, 2006
- [3] W. Cai, U.K. Chettiar, A.V. Kildishev, V.M. Shalaev, “Optical cloaking with metamaterials”, *Nature Photonics*, vol. 1, pp. 224-227, 2007
- [4] P. Alitalo, S. Tretyakov, “Electromagnetic cloaking with metamaterials”, *Materials Today*, vol. 12, iss. 3, pp. 22-29, 2009
- [5] V. G. Vesalago. “The Electrodynamics of Substances with Simultaneously Negative Values of ϵ and μ ”, *Soviet Physics Uspekhi*, vol. 10, no. 4, pp. 509-514, 1968
- [6] R.A. Shelby, D.R. Smith, S. Schultz, “Experimental Verification of a Negative Index of Refraction”, *Science*, vol. 292, no. 5514, pp. 77-79, 2001
- [7] D. Schurig, J. J. Mock, B. J. Justice, S. A. Cummer, J. B. Pendry, A. F. Starr, and D. R. Smith, “Metamaterial Electromagnetic Cloak at Microwave Frequencies”, *Science*, vol. 314, pp. 977-980, 2006
- [8] A. A. Houck, J. B. Brock, I. L. Chuang, “Experimental Observations of a Left-Handed Material That Obeys Snell’s Law”, *Physical Review Letters*, vol. 90, no. 13, pg. 137401, 2003
- [9] H. Chen, L. Ran, J. Huangfu, X. Zhang, K. Chen, T. M. Grzegorzcyk, J.A. Kong, “Left-handed materials composed of only S-shaped resonators”, *Physical Review E*, vol. 70, iss. 5, pg. 057605, 2004
- [10] B. Kante, D. Germain, A. de Lustrac, “Experimental demonstration of non-magnetic metamaterial cloak at microwave frequencies”, *Physical Review B*, vol. 80, pg. 201104, 2009
- [11] B. Ferguson, X. Zhang, “Materials for terahertz science and technology”, *Nature Materials*, vol. 1, iss. 1, pp. 26-33, 2002

- [12] B. Fischer, M. Hoffmann, H. Helm, G. Modjesch, P.U. Jepsen, "Chemical recognition in terahertz time-domain spectroscopy and imaging", *Semiconductor Science and Technology*, vol. 20, iss. 7, pp. S246-S253, 2005
- [13] P.H. Siegel, "Terahertz Technology", *IEEE Transactions on Microwave Theory and Techniques*, vol. 50, no. 3, pp. 910-918, 2002
- [14] J.S. Melinger, N. Laman, and D. Grischkowsky, "The underlying terahertz vibrational spectrum of explosives solids", *Applied Physics Letters*, vol. 93, iss. 1, pg. 011102, 2008
- [15] R.M. Woodward, V.P. Wallace, D.D. Arnone, E.H. Linfield, M. Pepper, "Terahertz Pulsed Imaging of Skin Cancer in the Time and Frequency Domain", *Journal of Biological Physics*, vol. 29, iss. 2, pp. 257-261, 2003
- [16] T. Löffler, T. Bauer, K.J. Siebert, H.G. Roskos, A. Fitzgerald, S. Czash, "Terahertz dark-field imaging of biomedical tissue", *Optics Express*, vol. 9, pp. 616-621, 2001
- [17] K. Humphreys, J.P. Loughran, M. Gradziel, W. Lanigan, T. Ward, J.A. Murphy, C. O'Sullivan, "Medical applications of Terahertz Imaging: a Review of Current Technology and Potential Applications in Biomedical Engineering", *Engineering in Medicine and Biology Society*, pp. 1302-1305, 2004
- [18] A.G. Davies, A.D. Burnett, W. Fan, E.H. Linfield, J.E. Cunningham, "Terahertz spectroscopy of explosives and drugs", *Materials Today*, vol. 11, iss. 3, pp. 18-26, 2008
- [19] D.L. Woolard, E.R. Brown, A.C. Samuels, J.O. Jensen, T. Globus, B. Gelmont, M. Wolski, "Terahertz-Frequency Remote-Sensing of Biological Warfare Agents", *Microwave Symposium Digest*, vol. 2, pp. 763-766, 2003
- [20] S. Dexheimer, "Terahertz Spectroscopy: Principles and Applications", CRC Press, Boca Raton, FL, 2008
- [21] R.F. Harrington, "Time-Harmonic Electromagnetic Fields", McGraw Hill, New York, NY, 1961
- [22] J. B. Pendry, A. J. Holden, D. J. Robbins, and W. J. Stewart, "Magnetism from Conductors and Enhanced Nonlinear Phenomena", *IEEE Transactions on Microwave Theory and Techniques*, vol. 47, no. 11, pp. 2075-2084, 1999
- [23] N.I. Landy, S. Sajuyigbe, J.J. Mock, D.R. Smith, W.J. Padilla, "A Perfect Metamaterial Absorber", *Physical Review Letters*, vol. 100, pg. 207402, 2008
- [24] H.Tao, N.I. Landy, C.M. Bingham, X. Zhang, R.D. Averitt, W.J. Padilla, "A metamaterial absorber for the terahertz regime: Design, fabrication and characterization", *Optics Express*, vol. 16, pp. 7181-7188, 2008

- [25] H. Tao, C.M. Bingham, A.C. Strikwerda, D. Pilon, D. Shrekenhamer, N.I. Landy, K. Fan, X. Zhang, W.J. Padilla, R.D. Averitt, "Highly flexible wide angle of incidence terahertz metamaterial absorber: Design, fabrication, and characterization", *Physical Review B*, vol. 78, pg. 241103, 2008
- [26] H. Tao, C.M. Bingham, D. Pilon, K. Fan, A.C. Strikwerda, D. Shrekenhamer, W.J. Padilla, X. Zhang, R.D. Averitt, "A dual band terahertz metamaterial absorber", *Journal of Physics D: Applied Physics*, vol. 43, iss. 22, pg. 225102, 2010
- [27] W.J. Padilla, M.T. Aronsson, C. Highstrete, M. Lee, A.J. Taylor, R.D. Averitt, "Electrically resonant terahertz metamaterials: Theoretical and experimental investigations", *Physical Review B*, vol. 75, iss. 4, pg. 041102, 2007
- [28] COMSOL Multiphysics 4.1, COMSOL, Inc.